Alma Mater Studiorum · Università di Bologna

Scuola di Scienze
Dipartimento di Fisica e Astronomia
Corso di Laurea in Fisica

STUDY OF NANOSTRUCTURED TARGETS FOR PLASMA PRODUCTION VIA LASER ABLATION

Relatore:
Prof. Marco Cuffiani

Correlatore:
Dott. Fabrizio Odorici

Presentata da:
Marco Frassetto

Anno Accademico 2016/2017

Abstract

This thesis studies the effects of pulsed laser irradiation (6 ns long, $4 \cdot 10^{12} W/cm^2$, 1064 nm wavelength) on different nanostructured targets, with the goal to produce a dense, hot plasma, of great interest for astrophysics and nuclear physics studies.

Targets used in this study are metamaterials consisting in aligned metal nanowires (NWs) grown by electrodeposition into a porous alumina matrix, obtained on an aluminum substrate. Targets were developed with different parameters, like length, diameter and metal, chosen to maximize absorption in visible and IR wavelengths and to study ablation depth and plasma X-fluxes.

Large differences in X-fluxes and ablation depth have been found, both comparing the nanostructured targets with bulk aluminum and among each other. In particular, Co NWs have been found to give a two-fold increase in X-ray flux compared to Ni and Fe.

A factor of five X-flux difference has been obtained when two different nanowires deposition techniques, alternate current vs direct current, are applied. For DC deposition, each NW is electrically connected to the aluminum substrate, while for AC deposition NWs are insulated by non-conductive alumina. These differences in X-flux and ablation depth can't be easily explained considering only the bulk properties of the elements involved, like different atomic number and thermal conductivity of the NWs metal. A possible explanation for the observed differences is that plasmonic effect plays an important role in laser energy absorption. Due to this effect, the light pulse is converted into an electrical pulse at the top of the NW and propagated along it.

Since NWs can be tens of µm long, energy can be transported deeply into the material. Such a deep penetration is not possible in bulk materials, where EM energy is absorbed within 100 nm. Thus, differences among targets could be explained considering plasmonic propagation length, which is dependent on geometrical parameters and electrical conductivity of the NWs.

Abstract

Questa tesi studia gli effetti dell'irraggiamento con impulsi laser (6 ns di durata, $4 \cdot 10^{12} W/cm^2$, lunghezza d'onda 1064 nm) di diversi bersagli nanostrutturati, con l'obbiettivo di ottenere un plasma denso e caldo che irradi un intenso flusso X.

I bersagli usati per questo studio sono metamateriali che consistono in nanofili allineati cresciuti per elettrodeposizione in una matrice di allumina nanoporosa, ottenuta su un substrato di alluminio. I bersagli sono stati sviluppati con parametri geometrici tali da massimizzare l'assorbimento nelle lunghezze d'onda del visibile e IR.

Per studiare quali parametri portino al Massimo flusso di raggi X, sono stati prodotti nanofili con diversi diametri, lunghezze, metallo e tecnica di deposizione.

Sono state osservate grandi differenze nei flussi di raggi X e nelle efficienze di ablazione, sia confrontando i bersagli nanostrutturati con l'alluminio bulk sia fra loro. In particolare, si è osservato che i nanofili di cobalto ottengono un flusso di raggi X doppio rispetto a quelli di Nichel e Ferro. Una differenza di cinque volte nel flusso di raggi X è stata ottenuta usando due diverse tecniche, deposizione in corrente continua oppure alternata. Nella deposizione in CC, ciascun nanofilo è in contatto elettrico con il substrato, mentre nella deposizione in AC i nanofili sono isolati da uno strato di allumina non conduttiva.

Queste differenze in termini di flusso X ed efficienza di ablazione non possono essere spiegate in modo semplice considerando solo le proprietà collettive degli elementi implicati, come il diverso numero atomico e la diversa conducibilità termica del metallo dei nanofili.

Una possibile spiegazione per le differenze osservate è che l'effetto plasmonico abbia un ruolo importante nell'assorbimento dell'energia laser. Grazie a questo effetto, l'impulso luminoso viene convertito in impulso elettrico all'estremità superiore del nanofilo e propagato lungo di esso.

Poiché i nanofili possono essere lunghi decine di micrometri, l'energia può essere trasportata in profondità nel materiale. Una penetrazione così profonda è impossibile in un materiale bulk, dove l'energia viene assorbita entro i primi 100 nm.

Quindi, le differenze fra i bersagli potrebbero essere spiegate considerando la lunghezza di propagazione plasmonica, che dipende dai parametri geometrici e dalla conducibilità elettrica dei nanofili.

Contents

0.1 Introduction

Nanostructured materials have been studied and produced for a wide range of applications. In this thesis optical and electrical properties of metal nanowires - i.e. wires smaller than 100 nm in diameter and up to tens of μm long - are used as targets for plasma production with a pulsed laser, in the ns domain, power density of about $4{\cdot}10^{12} W/cm^2$ and wavelength 1064 nm.

Metal nanowires exhibit a peculiar opto-electronic behaviour called plasmonic effect: they act as waveguides for light with wavelength much greater than their diameter, absorbing incident light at one end, transporting it as a collective excitation of free electrons (plasmon), and reemitting it as light at the opposite end.

Therefore, nanomaterials with a dense population of vertically aligned metal nanowires can be very effective in absorbing incident light. To create such materials, a multi-steps process is used. First, aluminum is anodized in specific electrochemical condition which lead to self-organization of regular and vertical empty pores in the oxide layer that is formed. Second, a given metal (such as Ag, Fe, Co or Ni) is used to fill these pores with electrodeposition, forming a population of densely packed, highly regular nanowires normal to the surface.

This nanostructured material can be useful as a target for laser plasma formation. On the other hand, laser-produced plasma, which is hot and near solid in density, is interesting both as an intense X-source for imaging purposes and for the study of nuclear processes in near astrophysical conditions. But while in an ordinary target, the laser energy is absorbed in a very thin (hundred of nm) layer at the target's surface, nanostructured targets can absorb more electromagnetic energy and transport it deeper inside the material, forming a plasma which is expected to have higher density and temperature.

This thesis work was part of preliminary data taking for a future experiment, aimed at developing new nanomaterials optimized for laser plasma production. This thesis is dedicated to the study of laser irradiation of nanostructured targets with different nanowires parameters (i.e. metal, length, diameter).

Comparison between irradiation of different targets is based on two types of data: X-ray fluxes emitted by the plasma during irradiation, and morphological analysis of craters formed on the laser irradiation sites. This morphological analysis was performed as part of this thesis work, using a 3D scanning optical microscope.

The first chapter describes the state of the art for the different involved fields: the technology for the production of regular and aligned metal nanowires, current understanding of energy transport by plasmonic effect in nanowires, and finally laser-matter interactions for ordinary targets and their in limit in electromagnetic energy absorption

which nanomaterials could overcome.

The second chapter describes the experimental setup and procedure used for this work's measurements. This includes the description of the tested samples along with the process for their production, the setup used for irradiation of targets, and finally the instruments employed to collect X-rays and morphological data.

The third chapter presents the data used for comparison of targets, including the morphology of the craters formed by laser irradiation. Uncertainty calculation and rejection of unreliable data are also discussed.

In the fourth chapter data from different targets are compared, with respect to other nanostructured targets or bulk aluminum (used as a control sample), in order to determine which kind of targets provide the best performances, in terms of largest X-ray flux and deepest craters. Finally, future developments for this research will be discussed.

Results from this study will be the first step toward optimization of nanostructured targets for future experiments.

Chapter 1

State of the art

1.1 Nanostructured materials

Nanostructured materials - materials engineered with features smaller than a μm - have attracted a great deal of interest in recent years for scientific and technological applications in a wide range of contexts - drug delivery, sensors, optics, electronics and more.

Until recent years the most common techniques used for nanofabrication were microlithography, ion or electron beams. They allow great control over the process, but are severely hampered by high cost, low throughput, and resolution limits [1].

This led to great interest in developing cost-effective, robust and controllable fabrication processes for nanomaterials production. In recent years, new physical and chemical techniques have been demonstrated and employed to fabricate nanostructures in a wide range of shapes (sphere, ellipsoids, pillars, tubes, wires, cones...) and sizes.

Of particular interest to us is the fabrication of metal nanowires (NWs). A very effective strategy for NWs fabrication which emerged in recent years is electro-chemical deposition in Porous Anodized Alumina Templates. In this process, first an alumina template with deep and regular-shaped channels normal to the surface is created. Then, the channels are filled with metal through electrodeposition. Changing anodization and deposition conditions allows control over the resulting NWs shape and structure. Many different metals can be deposited this way: iron, copper, gold, silver, nickel and cobalt NWs have been fabricated this way[2, 3].

This comparatively simple and inexpensive technique allows fabrication of NWs with excellent regularity, crystallinity and aspect ratio, while allowing high throughput and scalability [4].

In the rest of this subsection, the techniques for making alumina templates and filling the channels with metal will be discussed.

1.1.1 Anodized Alumina Templates

Porous Alumina (aluminum oxide, Al_2O_3) coatings were initially employed for decorative and protective purposes, due to their hardness and resistance to corrosion [5]. In the last decade, they emerged as powerful tools for fabrication of nanostructures, thanks to the their regularly shaped nanoscale channels (pores).

Anodization parameters (applied voltage or current, pH, type/concentration of the electrolyte, and temperature) affect the features of the resulting alumina film in different ways. First, anodization can either form a continuous barrier type, parallel to the aluminum surface, and a porous barrier, which is the one of interest for NWs fabrication. While neutral or basic electrolytes lead to continuous barrier formation, an acidic electrolyte generates a porous barrier, thanks to the competition between electric field driven oxide formation, which happens at the metal-oxide interface, and oxide dissolution at the electrolytic-oxide interface [4]. Most common acid electrolytes are based on sulfuric, oxalic or phosphoric acid.

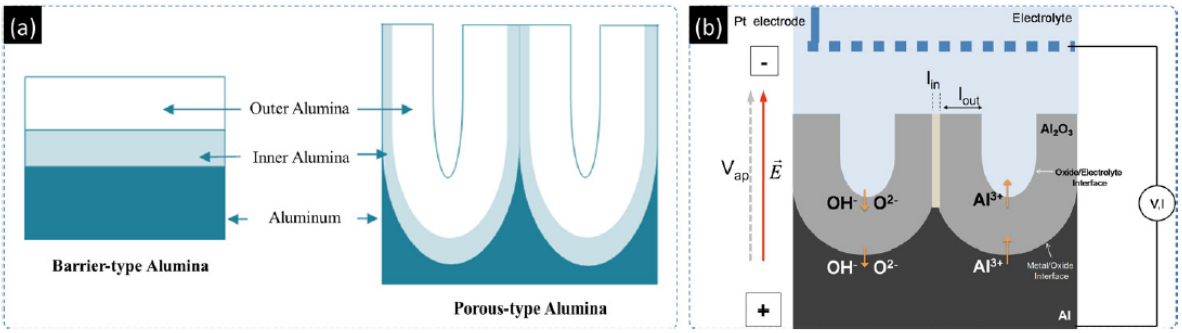

Figure 1.1: (a): Different types of alumina coating. The continuous type alumina is not useful for nanotechnology purposes, while the porous kind is useful for NWs fabrication. (b):Pores - also called channels - formed in porous alumina. Note that an oxide layer (grey) separates the empty channels from the metallic aluminum (black) [1].

While the exact reactions involved are rather complicated and subject to some debate, the occurring electrochemical processes at the anode can be simplified to:

$$Oxide\ formation : 2Al_{(s)} + 3H_2O_{(l)} \rightarrow Al_2O_{3(s)} + 6H^+_{(aq)} + 6e^- \tag{1.1}$$

$$Oxide\ dissolution : Al_2O_{3(s)} + 6H^+_{(aq)} \rightarrow 2Al^{3+}_{(aq)} + 3H_2O_{(l)} \tag{1.2}$$

As represented in figure 1.1, the alumina produced this way has two different regions. The inner, closer to the metal, is denser and more pure, while the outer, closer to the oxide-solution interface, is less dense and substantially anion contaminated [6].

The pores - or channels - created this way are perpendicular to the surface and have

a narrow distribution of diameter and length. Due to this, they can be used as "guides" for deposition of metals, allowing the fabrication of nanowires [7].

An important property of Alumina Templates is *self-organization*: channels are regular in shape and spatial distribution, with a honeycomb-like hexagonal cell structure(see figure 1.2. While there is not yet a consensus over the process behind this pattern, it is thought to be related to an effective repulsive force between the origin points (roots) of the pores. From experimental data and some models, a porosity (percentage of "empty" volume) of about 10% is essential to obtain self-ordered pores [8].

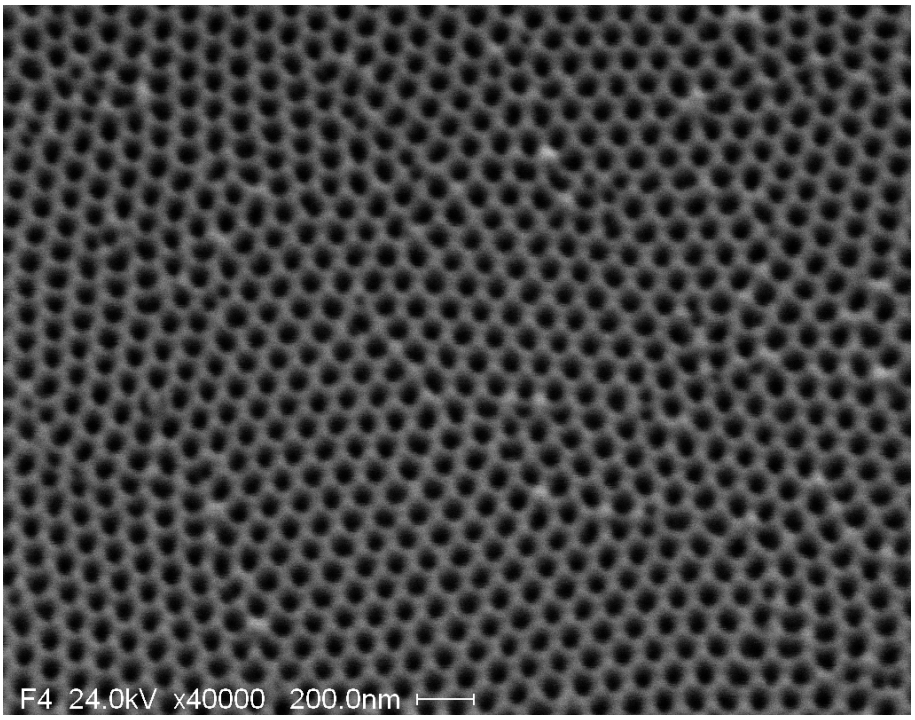

Figure 1.2: SEM image of nanoporous alumina, seen from above. The very regular honeycomb structure of channels can be noted. In this case, pores are about 60 nm in diameter, but considerably smaller ones, down to 20 nm, can be obtained

The hexagonal cell structure's degree of order depends on purity of the aluminum, electrolyte choice and concentration, temperature and metal grain size. If a highly regular array is required, thermal annealing (heating and then slowly cooling the material) can increase the metal's grain size, while two-steps anodization (chemically removing the oxide layer and repeating the anodization process) leads to much more regular hex cells [7, 9, 10]. For our needs, regularity of the array is not crucial and single step anodization is used.

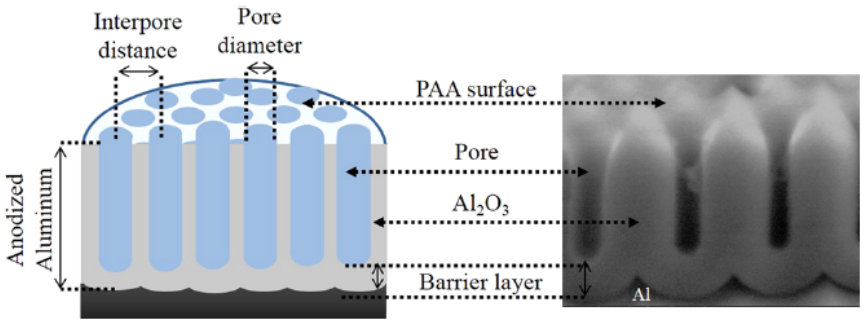

Figure 1.3: Diagram (left) and cross-sectional SEM image (right) of the pores formed by ordered alumina growth. Note the barrier layer formed under the pores [1].

Several important parameters of the template can be controlled, to some extent, by anodization conditions. The most important are barrier thickness, pore diameter and oxide layer thickness. We will now consider how these parameter can be controlled and the range of values which can be obtained [1, 6].

Geometrical parameters: the main geometrical parameters of the alumina template are: [9]

- Interpore distance d_{int}, the distance between the centres of adjacent pores
- Pore diameter d_p
- Barrier thickness, the thickness of continuous oxide layer at the bottom of channels
- Wall thickness, the thickness of oxide forming a channel's "walls"

Interpore distance is proportional to anodization voltage V_{ap}, being connected by the simple relation:

$$D_{int} = 2.5V_{ap} \tag{1.3}$$

which has been shown to be valid for a wide range of electrolytes and potentials (see fig 1.4)

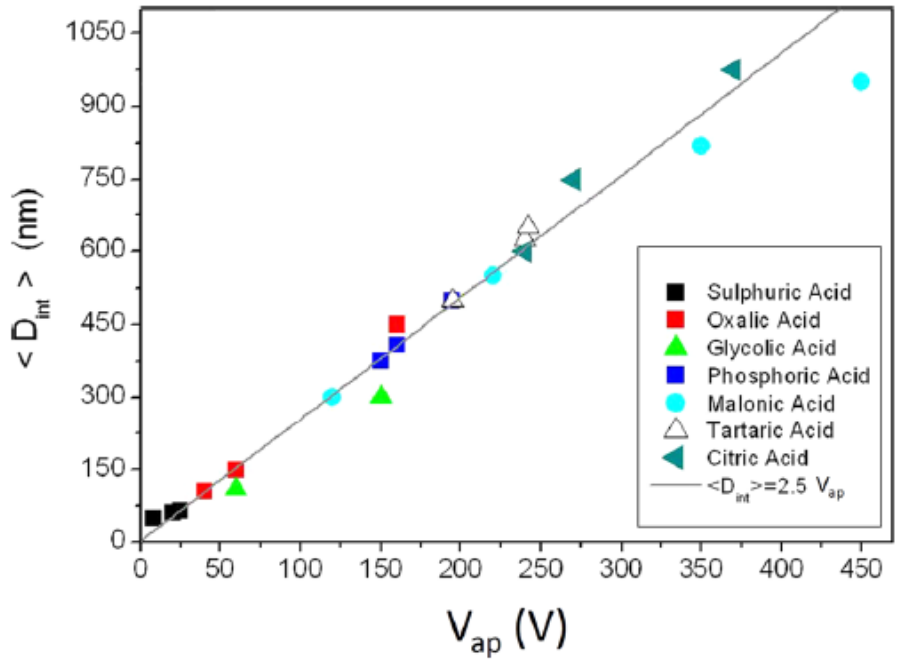

Figure 1.4: Experimental data for interpore distance vs anodization voltage. As can be seen, they are directly proportional over a wide range. The proportionality constant is in the order of 2.5 nm/V. Different voltage ranges require use of different acids. This work's interest is limited to small diameter NWs, therefore only sulphuric and oxalic acid (black and red points) have been used [1].

Pore diameter, being closely related to interpore distance, is also proportional to anodization voltage, with a proportionality constant on approximately 1 nm/V.

The above considerations sharply limit the available range of diameters for a given electrolyte, since anodization voltage must be high enough to reach the self-organization regime but not so high the barrier thickness completely blocks conduction, thus making electrodeposition of NWs impossible [1].

Taking all this into account, the main way to control D_{int}, and pore diameter with it, is to use a different electrolyte. Stronger acids lead to smaller pores. Of greatest interest for sub-visible wavelength applications are sulphuric, oxalic and phosphoric acyds. In table 1.5 optimal anodization conditions and resulting parameters are shown. As can be seen, pore diameters ranging from tens to hundreds of nm can be obtained with different electrolytes, but for a given electrolyte the window of anodization conditions is quite narrow.

For a given D_{int}, pore diameter can be somewhat enlarged by chemical pore widening - that is, cutting off the anodization current leaving the sample in the solution, allowing the acid to attack pore walls and thus increasing pore diameter.

Acid	Sulfuric	Oxalic	Phosphoric
Potential (V)	25	40	195
Concentration (M)	0.3	0.3	0.1
$\langle D_{int} \rangle$ (nm)	65	105	480
$\langle D_p \rangle$ (nm)	25	35	180
t_b (nm)	~34	~50	~250
Porosity (%)	~14	~10	~13
Velocity (μm/h)	5	2.5	5
Temperature (°C)	~1	~4	~1

Figure 1.5: Typical conditions for aluminum anodization using different electrolytes. Temperature, voltage and concentration cannot be changed too much without losing self-organization. Therefore, to create templates with different parameters, different acids are used.

As will be shown later, these parameters directly impact the formation of nanowires, which will inherit the pores'geometry.

Anodization current over time: the time dependence of the anodization current density j(t) during PAA formation is well established and can also provide insights into the growth process. As shown in figure 1.6, four different stages of anodization can be distinguished [7, 1]:

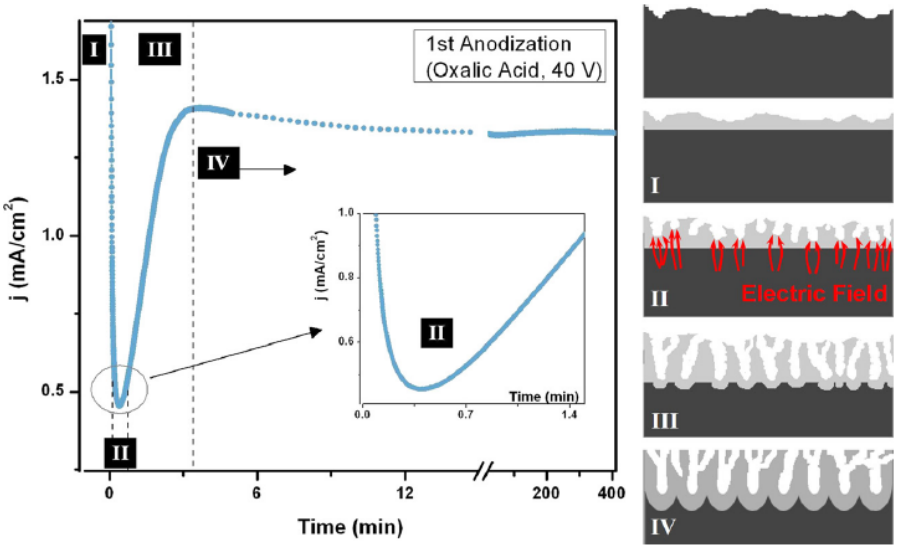

Figure 1.6: Typical behaviour of anodization current over time for oxalic acid anodization. While oxide layer growth rate is different for different electrolytes, the [1]

- **Stage I:** at the beginning of the anodization process, the formation of an oxide barrier layer with high resistivity causes a sharp decrease in j(t).

- **Stage II:** surface irregularities lead to focusing of electric field lines at specific points. This gives rise to localized heating by electrical dissipation. Higher temperature enhance chemical dissolution of the oxide layer, thus decreasing resistivity. Soon a balance is reached between oxide growth and dissolution, and j(t) reaches a minimum value.

- **Stage III:** intense dissolution sites nucleate into pores, and channels begin forming. Channels allows ions passage, so j(t) grows quickly to a maximum value.

- **Stage IV:** as channels grow and some close off, j(t) slowly decreases and finally reaches an almost constant value when an equilbrium between dissolution and growth is once again found. From this point, the oxide layer grows at a constant rate.

Note that, no matter the depth of the pores, a thin layer of continuous barrier-layer is always present at the bottom of each nanopore [6].

Oxide layer thickness: the thickness of the oxide layer (channels included) is mainly determined by anodization time [11]. Longer anodization leads to a thicker alumina layer, in an approximately linear fashion. Thicker oxide layer means deeper channels, allowing formation of nanowires with a higher aspect ratio (lenght divided by diameter). Channels tens of μm high can be consistently achieved.

It should be noted that while alumina is more dense than aluminum, its volume is not 100% solid due to porosity (which is around 10% for optimal anodization conditions), and mass is gained in the process (more oxygen is gained than aluminum is lost). Thus, anodization increases an object's volume, "swelling" its surfaces [8].

1.1.2 NWs electrodeposition

Once a nanoporous matrix with the desired geometry has been obtained, it can be used to grow nanowires inside the pores.

The electrodeposition method basically consists in the growth of a metallic material on top of a conducting substrate, by the electrochemical reduction of metal ions present in an electrolyte solution. The general electrodeposition reaction can be expressed as:

$$\left(M_x W_y\right)^z + nxe \rightarrow xM^0 + yW \tag{1.4}$$

Where M is the metal to be deposited, W is an ion or molecule bound to the metal ion (usually H_2O or SO_4^{2-}), z is the charge of the $\left(M_x W_y\right)$ complex and n is the amount of electrons involved in the reaction.

Since a fixed number of metal ions is deposited per moved electron, the total deposited mass is proportional to the total transferred charge, which can be estimated measuring and integrating the electrical current during che deposition process. By Faraday's law of electrolysis, deposited mass m is:

$$m = \frac{QA}{nF} \tag{1.5}$$

Where Q is transferred charge in Coulomb, A is atomic mass in g/mol, n the stechiometric coefficient in 1.4 and F is Faraday's constant (96 485 C/mol).

Since NWs diameter is fixed by pore diameter, an immediate consequence of eq. (1.5) is that NWs length grows at a constant rate if deposition occurs at constant current.

However, alumina is non conductive, therefore the barrier layer at the bottom of the pores prevents electrodeposition using DC current. Two solutions are possible: either AC deposition is used, or the barrier must be opened.

AC deposition is possible because the barrier acts in a similar way to a capacitor and current rectifier, allowing growth of nanowires in the pores. NWs deposited in AC are insulated from each other and the aluminum substrate.

To remove the barrier and allow DC deposition, the whole oxide layer can be detached from the aluminum substrate, and the barrier can be removed from the bottom via mechanical or chemical means, but this requires a thick oxide layer to survive the process. If the opened pores are subsequently coated with metal on one side, this allows DC deposition, but requires a thick oxide layer to survive the process.

A different approach to barrier layer opening is electrochemically etching the barrier from the pores side. This requires very controlled conditions, to avoid destruction of the pores' walls, but if successfull, DC deposition can subsequently be used to grow NWs independently of total oxide thickness, and without detachment from the bulk aluminum. It should be noted that, once the barrier layer is opened, nanowires deposited in DC will contact the aluminum substrate directly, thus affecting the electrical behaviour of the resulting material.

1.2 Plasmonic waveguides

Nanowires can be fabricated with a much smaller diameter (< 100 nm) than visible light's wavelength. Sub-wavelength metallic structures interact with light in a much different way compared to macro-scale structures of the same material. This is due to a phenomenon called plasmonic effect, which has attracted great interest in recent years for its application in nanoscale manipulation of light.

Plasmons are collective electron excitations formed on the surface of metals, caused by electromagnetic radiation. Due to plasmonic excitations, a metal nanowire exposed to electromagnetic radiation acts as a waveguide, despite being much smaller than the incident wavelength: photons can be absorbed at one end of the nanowire, transported through its length as an electrical impulse, and re-emitted as photons (with some loss in intensity) at the opposite end [12, 13].

Plasmonic effect can be demonstrated observing the light-guide behavior of sub-wavelength metallic structures, but plasmons can also be directly imaged with near-field microscopy thanks to the strong electrical field they form near the metal surface, as can be seen in figure 1.7:

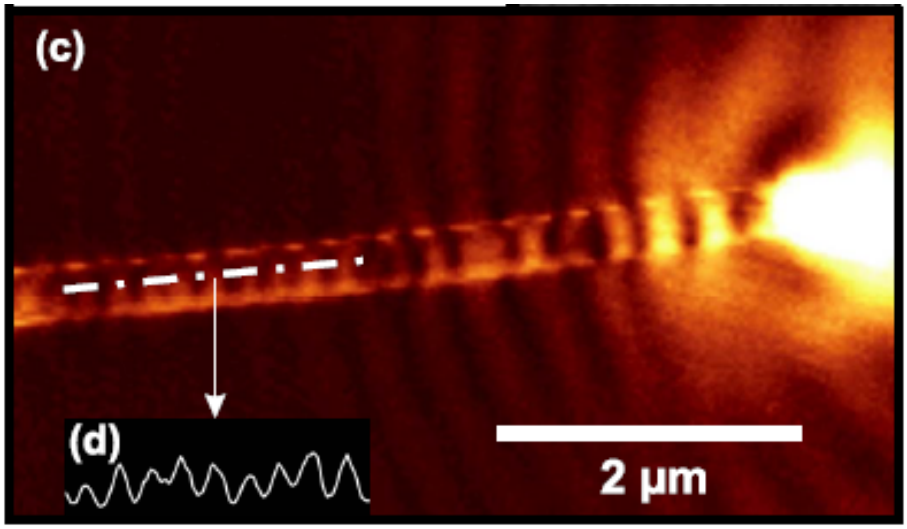

Figure 1.7: Surface plasmon oscillations imaged with Scanning Near Field Optical Microscope [20].

Plasmonic effect even works with bent nanowires and allows fan in-fan out. Thanks to these properties, metallic NWs are of great interest for many applications, from opto-electronic circuitry (as light guides with components much smaller than light wavelength) to sensors [14] and energy production [15].

Most important to us, is the capability of plasmonic effect to transfer energy delivered by laser beam from the surface to the interior of a target. This allows volumetric instead of superficial heating of matter, which is of great interest for dense plasma formation. Most of this thesis' work is aimed at comparing the plasmonic effect in different nanomaterials.

1.2.1 Plasmonic coupling to light

Light transmission through nanowires much thinner than wavelength has been repeatedly demonstrated and studied in recent years [16]. Impressive images directly demonstrating light absorption and emissions at the ends of a nanowire have been obtained,

such as 1.10.

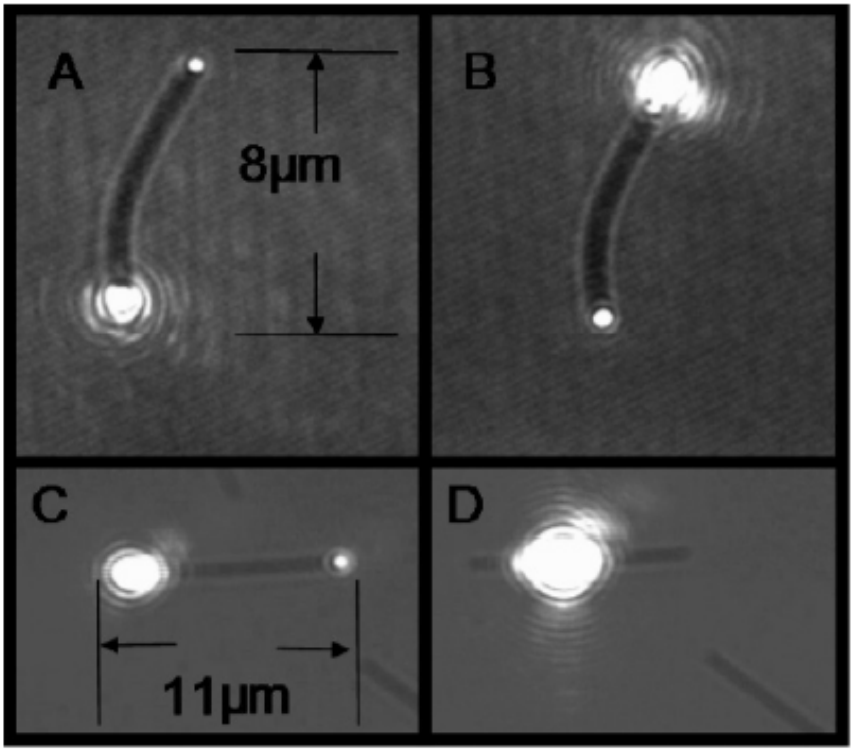

Figure 1.8: Light transmission through a metal nanowire thanks to the plasmonic effect. As can be seen, focusing light on one end of the NWs (A, B and C) causes emission at the opposite end, while focusing light on the middle of the NW (D) there is no emission, since plasmon excitations couple with photons only at discontinuities [16].

Light couples to plasmons at discontinuities. These are usually the ends of the NW, but can also be kinks or anisotropies along the wire. A gentle bend will not emit light, but will cause loss of energy, with greater loss at smaller radii [16]. This is of little concern in our experiment, since alumina-fabricated nanowires are very regular in shape and structure.

Plasmons, which can be treated as quasiparticles, propagate with specific wavelength and polarization, and nanowires have their own resonant frequency, which is strongly dependent on geometrical characteristics of the nanostructures. Therefore, photon-plasmon coupling is dependent on wavelength, and nanostructures' parameters can ben tuned - at least in principle - to absorb specific wavelengths [12].

The change in photon-plasmon coupling for different nanostructure geometry can be seen quite spectacularly observing the colour change in our samples for different heights of nanowires. As can be seen in image 1.9, there is a specific progression:

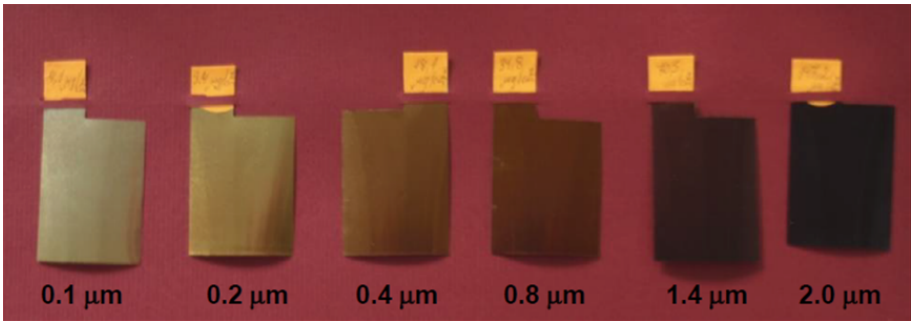

Figure 1.9: Change in light absorption for samples with NWs of different length. From left to right, the sample in this image have progressively longer NWs, from 0.1 to 2.0 μm. As can easily be seen, the longer the NWs, the darker the colour.

- Porous alumina without nanowires, or at very low NWs length, shows the colour of the aluminum substrate.
- For longer ($> 0.1\mu$m) nanowires, light is absorbed unevenly across the visible spectrum, thus colouring the sample. Different nanowires material give rise to different colours.
- For much longer ($> 2-3\mu$m) nanowires, the sample appears black, with absorption coefficient as high as 95%.
- When the growth of the nanowires exceeds the thickness of the alumina, the longest nanowires reach the top of the channels and start "overgrowing", forming characteristic mushroom structures. These irregularities break the photon-plasmon coupling, and the sample shows the colour of the nanowires metal. Obviously, this behaviour is undesirable and growth time should be adjusted to prevent it [18].

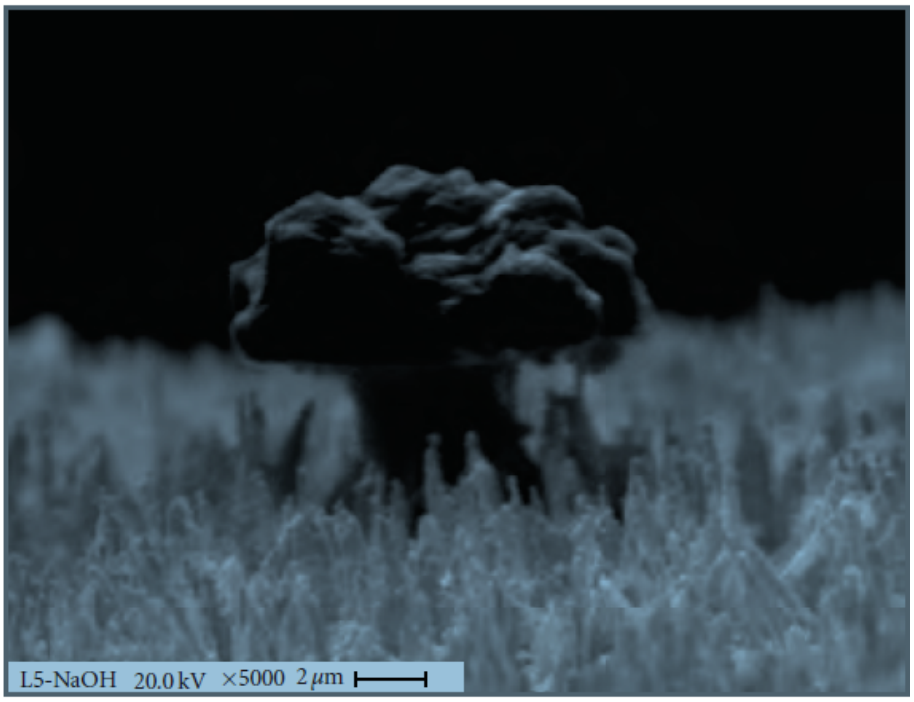

Figure 1.10: Ovegrowth of cobalt NW. Once a NW length exceeds that of the channel, it grows irregularly, forming a a "mushroom" [18].

Light absorption of nanowires is - unsurprisingly - dependent on incidence angle, favouring absorption along the NW axis. This is favourable for our applications, since alumina pores (and thus nanowires grown in them) are normal to the surface, and will transport light deep inside the material.

The specific absorption spectrum of nanowires is dependend on a great number of parameters, such as geometry, NWs metal and surrounding material (NWs freed from alumina have a remarkably different behaviour) [12, 17].

1.2.2 Energy transport by plasmonic effect

Of great interest to us is the capability of plasmonic effect to transport energy along the nanowire. As mentioned before, energy can be lost due to photon emission at discontinuities, but most of the energy loss is caused by ohmic heating of the nanowire. In our attempt to optimize volumetric heating of the material, this is a key property of the NWs.

A useful parameter to quantify energy loss is propagation length, defined as the length along which the propagating plasmon reduces its intensity by a factor e. Measuring propagation length in nanowires is tricky, due to the difficulty of manipulating single NWs and measuring the intensity of output photons.

Despite this, in recent years measurements have been successfully performed, and

theoretical models have been proposed, providing some information of interest for this work [16, 19]:

- Even minor differences in NWs parameters (geometry, material, surrounding material) lead to considerable differences in propagation length. Still, values range between few μm and tens of μm [16].
- Propagation length is considerably greater for highly crystalline (ideally monocrystalline) NWs. Thus, chemically deposited nanowires (such as those used for this work) have usually longer attenuation length than those fabricated via lithography.
- Propagation length is sensitive to wavelength, with longer attenuation length at higher wavelengths (see fig 1.11). This is encouraging, since a near infrared laser was used for this experiment.
- Propagation length is greater for NWs of greater diameter.

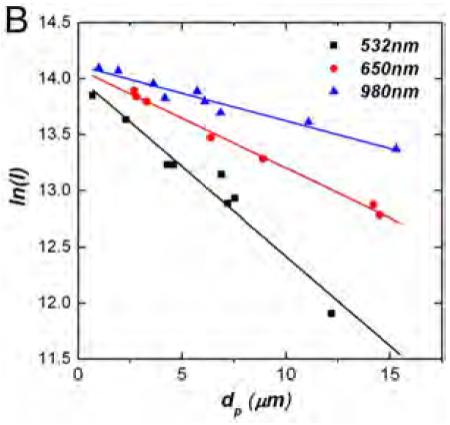

Figure 1.11: Intensity of light after propagation through NWs of different length. As can be seen, intensity decays exponentially with length. The slope is determined by propagation length. As can be seen, propagation length is longer for greater wavelength [19].

1.3 Laser-matter interaction

Laser heating of matter to obtain hot and dense plasma is of great interest for its applications in many fields, for example micromachining, X-rays production, nuclear physics and acceleration of charged particles.

Laser Produced Plasma (LPP) can easily reach densities orders of magnitude above any currently attainable magnetic confinement plasma, but is limited by a short lifetime: dense and LPP expands hydrodynamically and maintains densities of interest for nuclear processes for few nanoseconds at most.

During plasma cooling, a high flux of X-rays is emitted, which makes LPP a promising source for imaging and diagnostic, more energetic and bright than X-ray tubes and much more compact compared to accelerators [27].

The possibility to obtain LPP with greater energy content and longer confinement time is of great interest for all aforementioned applications. Unfortunately, there is a fundamental limit in the absorption of laser energy into matter: laser light penetrates very little into ordinary matter (tens of nm at most). Therefore, during laser irradiation of ordinary matter, only a thin skin of dense plasma is formed. This first layer of plasma prevents any further heating of the target, because dense plasma reflects very efficiently electromagnetic radiation [21]. Due to this, only a fraction of a laser pulse energy heats the target, forming a thin layer of dense plasma, which quickly cools due to expansion [22].

All mentioned application of LPP would benefit from a deeper heating of the target. With a volumetric instead of superficial heating, a longer-lived, denser and likely hotter plasma could be obtained from a laser pulse.

Thanks to its light-guide behaviour, plasmonic effect could allow a deeper penetration of light into matter. Incoming laser light, instead of heating only the first few tens of nm of the target, could convert its energy to heat within several propagation lengths (1μm). Recent literature, and this work's observations, show a greatly increased X-ray flux for nanostructured targets compared to Al-Bulk ones [23, 24].

The behaviour of a LPP, especially in a complex medium like a nanostructured target, is very difficult to understand in detail. Simulations are very complex even when using several approximations, and data are difficult to gather and analyze. Still, understanding the processes involved in energy transfer to and from LPP is necessary to understand the potential advantages of nanostructured targets.

1.3.1 Light absorption

Several different physical processes come into play in heating the target, their relative importance depending on time and thermodynamic conditions [27, 21].

Initial stages: before plasma formation, laser energy is absorbed by electrons in the target. For a flat metal target, this phase is dominated by the optical absorption length, which is few nm in most metals. Above a certain material-specific threshold fluence - i.e., a given amount of deposited energy per surface unit - violent vaporization occurs [26].

If the threshold energy is delivered in a short (sub nanosecond) time scale, vaporization does not occur through "normal" nucleation of bubbles, but a different process called "phase explosion" [25]. In phase explosion, temperature briefly rises above critical

temperature, but if the process is fast and the metal regular, instead of bubble nucleation at irregularities, homogeneous nucleation occurs, leading to violent expulsion of metal vapor and liquid droplets. Still, due to the low penetration of light into the target, only a thin layer is ablated [22].

It must be understood that not all of the ablated material becomes ionized, or even vaporized. Since the fusion energy of most metals is much lower than their evaporation and ionization energy, this must be taken into account when the energy balance of the process is considered.

After vaporization (which occurs in times much shorter than a nanosecond for a high power laser), the gas starts ionizing, and light absorption mechanisms change [21, 27].

EM wave propagation: the absorption of light strongly depends on laser parameters such as intensity and wavelength. When the field of the laser is strong enough it will force electrons to oscillate with a velocity, given by

$$v_{osc} = \frac{e \cdot E}{m_e \omega} = \sqrt{\frac{I \cdot \lambda^2}{1,39 \cdot 10^{10 W/cm^2}}} \tag{1.6}$$

where I is laser intensity and λ is wavelength. Due to the factor $I \cdot \lambda^2$, the dominating process of energy transfer changes with the product $I \cdot \lambda^2$. The most important heating processes are:

- **Inverse bremsstrahlung:** dominating at comparative low $I \cdot \lambda^2$, it is the collision of photons with free electron in plasma.
- **Resonant absorption:** in this process, which becomes important over $I \cdot \lambda^2 = 10^8$ W, the electric field of the laser pulse perpendicular to the target surface creates a plasma density wave, which in turns heats the electrons within the plasma.
- **Vacuum heating:** this process dominates at very high intensities (over $I \cdot \lambda^2 = 10^{10}$ W). In vacuum heating, free and even bound electron at the edge of the plasma are ripped away during a half-cycle of the EM wave, and then accelerated back against the plasma, transferring energy to it.

All these processes are limited by a fundamental constraint: the ability of the EM wave to penetrate the plasma. When a plasma reaches sufficient electron density (about two orders of magnitude below that of a solid), it becomes almost perfectly reflective to electromagnetic radiation [22]. In Laser Produced Plasma, a steep density gradient forms near the solid surface, and when sufficient density is reached, a reflective critical surface forms.

The mirror-like behaviour of a critical surface (see figure 1.12) sharply limits the possibility to heat matter with laser light. A very fast laser - pulse length shorter than a femtosecond - can deliver most of its energy before plasma is formed, but still it can reach only the surface of the target, since the pulse duration is too short to allow for thermal conduction.

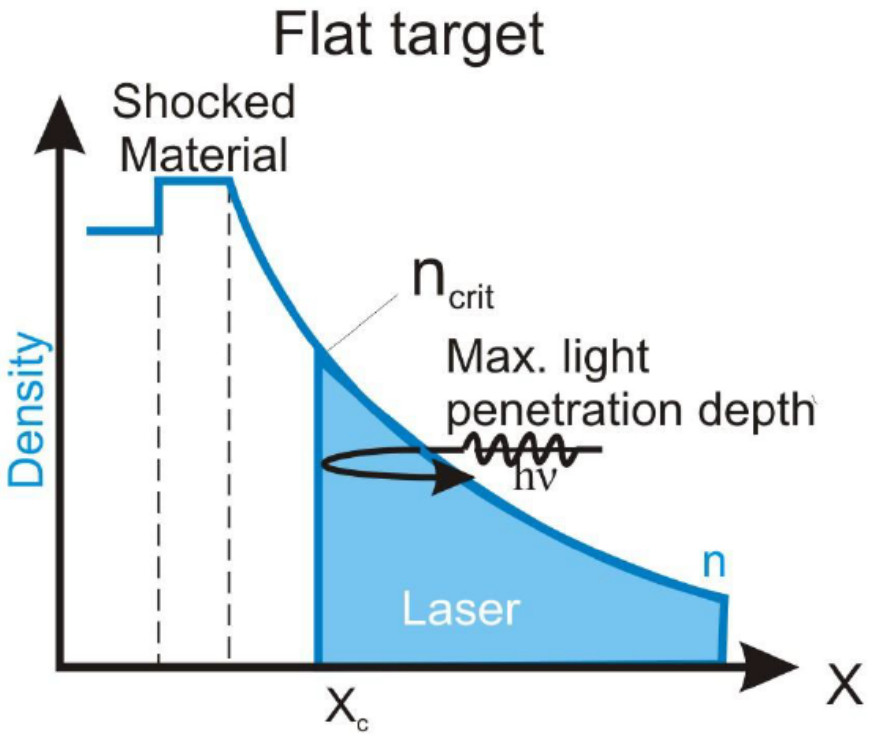

Figure 1.12: Light reflection on critical density plasma. As the incoming EM wave approaches the surface, it encounters denser and denser plasma, until critical density (which is two orders of magnitude lower than solid density) is reached and light is reflected back. Due to this effect, laser heating of a dense plasma is very inefficient [21].

This is the limitation which nanostructured targets could overcome. As explained in previous sections, nanowires normal to the surface absorb incoming photons and transport them deep into the material as plasmons. It is hoped this will provide an efficient process to deliver energy into a thick volume instead of a thin surface layer. Plasma produced in this way would have two advantages: less beam energy would be lost to reflection, and lower surface-to-volume ratio would make thermodynamic expansion slower.

1.3.2 Plasma cooling

The processes involved in plasma cooling are important for two reasons: understanding them is useful for plasma diagnostic, and many interesting applications for LPP (as X-ray source, for example) depend on the radiative cooling processes.

There are two main ways for a hot plasma to lose energy: hydrodynamic expansion

and radiative processes[21]. Each one works on a specific timescale which depends on density and temperature. The process with a shorter timescale dominates at given plasma parameters.

Hydrodynamic cooling: for a flat target, hydrodynamic cooling time can be defined as $\frac{\Delta_L}{c_s}$, where Δ_L is the plasma dimension (assuming a layer of plasma, of thickness L, which expand monodimensionally) and c_s is the speed of sound in plasma. The latter can be calculated as:

$$c_s = \sqrt{\frac{ZkT_e}{M_i}} \tag{1.7}$$

While this expression is simple, its result can be misleading: plasma production continues for several nanoseconds after the end of laser pulse, the geometry of the ablated crater plays a role in confinement of plasma, and the assumption of monodimensional expansion does not hold true for the intense laser pulses considered in this work. Yet, it is important to note that hydrodynamic cooling is strongly dependent on the thickness of the plasma layer.

Radiative processes: laser produced plasma can radiate away energy through several different process, each adding a contribution to the emission spectrum of the plasma. The main radiative processes are [21, 27]:

- **Line emission:** emission due to de-excitation of residual electrons in ions. Lines are broadened by excited states lifetimes and doppler effect. Lines due to this effect can be used to discern the atomic species in the plasma and their degree of ionization.
- **Recombination emission:** emission due to photorecombination of electrons and ions.
- **Brehmsstrahlung:** the well-known phenomenon of emission due to electrons collisions with ions is particularly important for low Z plasma (since ions are completely stripped). It contributes with a continuous exponential term to the spectrum, which can be used to calculate plasma temperature.
- K_α **emission:** this process can be observed if a population of highly energetic electrons (10-100 keV) is formed, for example due to resonant absorption. These fast electron can be reflected against the cold, unionized matter and strip the core electrons, thus leaving a hole which is filled by a transition at a very specific energy.

Since the resonance absorption process is more efficient for short-pulse generated plasma, K_α emission is more common in that kind of plasma.

Calculating the timescale for radiative processes is extremely difficult and depends on many unknown parameters. According to simulations performed in reference [21], for electronic densities above 10^{23} particles/cm^3 radiative lifetime becomes shorter than hydrodynamic, and the single largest contribution comes from line emission. At lower densities, hydrodynamic cooling is dominant, and brehmsstrahlung becomes the most important radiative phenomenon. Since LPP is near-solid in density, radiative and hydrodynamic cooling can be expected to be comparable in magnitude.

Therefore, a longer hydrodynamic lifetime (due to better confinement) would mean a greater total X-ray flux, and a longer "window" for study of nuclear processes which require a hot, dense plasma.

1.3.3 Crater morphology

An important source of data for this study is the observation of craters formed on the target after laser irradiation. Comparison of craters in different materials can give useful information on the difference in terms of energy penetration and plasma development.

Most research on laser ablation is focused on micromachining applications on pure metals [22], but it also provides useful data for this work's purpose. In the following paragraphs, some useful quantities for the study of craters will be defined, and the effect of different laser parameters on craters will be discussed.

Ablation threshold: to discuss the effects of laser irradiation of solid targets, it is useful to define "fluence". Fluence is calculated as intensity integrated over time (typically expressed in J/cm^2) and is one of the most important parameters for understanding laser-solid interactions [29].

Laser ablation - that is - that is, removal of matter from the target due to phase change - occurs over a given threshold fluence. This threshold depends on many parameters such as surface morphology, impurities, laser wavelength and properties of the target material, but for most metals is between 1 and 10 J/cm^2 [26, 22].

Below the ablation threshold, surface modification and some metal vaporization still occurr, but very little matter is removed and there is no plasma formation. Since the laser used for this work has a fluence on the order of 6000 J/cm^2, plasma formation is easily reached.

When ablation threshold is reached, different processes remove matter from the target. As previously mentioned, fast heating can lead to homogeneous nucleation and phase

explosion, with violent expulsion of molten and vaporized matter. If excitation time is shorter than thermalization time in the material, ablation can also occur through athermal processes, such as direct bond-breaking by laser light [25].

For metals, thermalization time is shorter than picosecond, and thus only relevant for ultrashort laser pulses. But dielectrics, such as alumina, have thermalization times ranging from tens of ns to μ. Since the target we employ are metal-dielectric metamaterials, it is unclear whether athermal processes play an important role in ablation [22].

After thermalization, ablation continues driven by the propagation of a shock wave in the target material. Due to this, plasma production can continue long after the end of the laser pulse [30].

Ablation efficiency: a quantity which is introduced to compare craters in different material or created by different laser beams, it is defined as the ablated volume divided by the delivered energy and usually measured in $\mu m^3/J$. For low energy pulses, ablation rate is proportional to the delivered energy, and ablation efficiency can also be calculated as depth divided by fluence [30]. It should be considered that most of the matter removed by laser ablation is not ionized, but simply expelled in gaseous or liquid phase. Therefore, greater ablation efficiency is not necessarily indicative of more plasma formation.

Crater depth and shape: crater shapes have been found to depend on laser beam diameter, laser pulse duration, energy, wavelength, target, and environmental conditions. Some of the most important dependencies will be discussed here:

- **Pulse duration:** for a given pulse energy, pulse duration strongly affects crater depth. Three different domains can be found: femtosecond, picosecond and nanosecond laser. The highest ablation efficiency is found for femtosecond laser, while the lowest for picosecond, rising again at nanosecond pulse duration. This is thought to be an effect of the different laser-plasma interactions. For femtosecond laser, pulse time is shorter than thermalization, and very little plasma is formed before the pulse ends. For picosecond laser, a dense plasma is rapidly developed, and a critical density surface forms, thus reflecting an important fraction of laser light. In the nanosecond domain, plasma is developed but it starts expanding, so more energy from the beam is either transmitted through the plasma or absorbed by it (in the latter case still indirectly contributing to ablation). The difference is greater for shorter wavelength, since a lower density is required for reflection [30, 31].

  Shorter pulse duration also leads to sharper shapes. In general, as the pulse length is shortened, energy is more rapidly deposited into the material leading to a more rapid material ejection. The volume of material directly excited by the laser has less

time to transfer energy to the surrounding material before being ejected. Therefore, the ablated volume becomes more precisely defined by the laser's spatial profile and optical penetration depth, and the remaining material has less residual energy, which reduces heat affected zone.

Note that this considerations have been demonstrated for metal target, but it is unclear if they apply to nanostructured target, since its interactions with laser light are likely to change when nanostructured are destroyed by thermal modifications.

- **Pulse energy:** Several studies have found ablation depth to correlate with the square root of energy[30]. Some models have been proposed to explain this dependency, and have been found predict experimental data quite well as long as plasma expansion can be considered one dimensional, which is usually valid for low energy (below mJ) pulses.

- **Laser wavelength:** At low fluence ($< 10^{10} W/cm^2$) short wavelength light leads to higher ablation efficiency. This is due to photochemical processes occurring at higher photon energy. For higher fluences, wavelength seems to have little impact on the ablation depth, except for phenomena related to laser-plasma coupling as previously exposed.

- **Target material:** For pure metals, the main difference in crater size is simply due to melting point and vaporization energy. Of the common metals, aluminum, lead and tin usually yield the highest ablation efficiency.

Chapter 2

Experiment

In this chapter, the experiment will be described. In the first section, the samples considered for this work will be described and compared. In the second, the irradiation procedure and setup will be detailed.

Since this thesis deals with the preliminary tests for an experimental research, during its realization some setup issues were identified. Therefore, in the last section some improvement which were made to the experimental setup and procedure will be explained.

2.1 Samples preparation

All of the samples considered for this thesis, and most of those used for preliminary studies, were produced at the INFN nanotechnology lab in Bologna. They were produced through electrodeposition (AC or DC) of metals in nanoporous alumina templates, as described in the first chapter.

2.1.1 Techniques

Anodization: highly pure aluminum samples were anodized in sulphuric or oxalic acid solutions (depending on desired diameter) to produce alumina templates. Since regularity of the pores disposition is not thought to be a key factor for this study, single-step anodization has been used. The solution was thermostated at 15 °C for most samples, leading to a growth rate of the oxide layer of approximately 5 μm per hour.

Electrodeposition: most nanowires were realized filling the pores via AC deposition. This way, the intact oxide barrier below the pores' root acted as capacitor and ion current rectifier, allowing the growth of metal nanowires in the as-grown template. For DC deposition, the barrier layer was opened via chemical and electrochemical attack

from the pores side. In such a case, NWs are grown in direct electrical contact with the aluminum substrate.

Control samples: each sample was anodized (and filled with NWs) along with a smaller control sample cut from the same aluminum sheet, to be used for quality control. This control sample, which is expected to have identical nanostructures to the main sample, can be used for destructive analysis (for example, cutting it to observe its cross-section with SEM) to directly observe the size and quality of nanostructures.

2.1.2 Samples

Before this thesis' work begun, preliminary data had already been collected from irradiation of a small number of samples. Some of the targets used for this preliminary data had been produced by the INFN lab in Bologna, while some were commercially available.

Preliminary data were used to compare the ablation of nanostructured samples versus bulk aluminum, and to test the experimental procedure. While data from these samples were sufficient to establish the advantage of nanomaterials compared to bulk aluminum, imperfect laser focusing (as will be described later) made the comparison between these samples unreliable.

While preliminary data will be mentioned when useful, this thesis' work is focused on (and mainly contributed to) the data taking which happened in April 2016.

All samples used in this data taking were 30 by 75 millimeters in size, and were anodized on both sides, leaving only a strip of bulk aluminum on the short side, by which it was held suspended in the solution during anodization and deposition. The bulk aluminum strip was also used to label samples. An example can be seen on figure 2.1. Craters were shot 2.5 mm apart, and the movimentation system allowed a 26 mm movement range in the transversal plane, allowing up to 100 shots per irradiation. Due to various geometrical constraints, at most 70-80 shots were actually fired per sample.

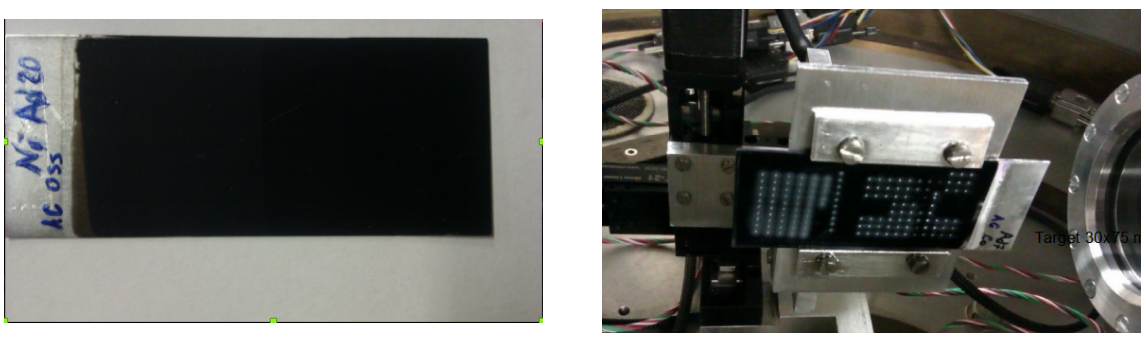

Figure 2.1: Typical sample before (left) and after (right) irradiation. After irradiation, the sample can be seen secured to the sample holder, and craters are visible as lighter spots.

For the data taking, several new samples were produced, aiming to get comparable samples for all the main variables of interest: nanowires composition, alumina thickness, nanowires height, nanowires diameter. A sample of bulk aluminum was also irradiated, to be used as reference.

Since preliminary data seemed to suggest deeper ablation for nickel NWs compared to cobalt and iron, most of the samples were filled with nickel. As will be discussed in the next chapter, more reliable measurements showed different results.

In table 2.1 specifics of samples are shown.

Sample name	NWs metal	Support label	NWs ⌀ (nm)	NWs length (μm)	Alumina thickness (μm)	Metal contact	NWs confinement
Al-Bulk	Al bulk	Al02	-	-	-	-	confined
Co-Thin	Cobalt	Ad7	20	10	10	NO	confined
Ni-Thin	Nickel	Ad3	20	10	10	NO	confined
Fe-Thin	Iron	Ad10	20	10	10	NO	confined
Ni-Long	Nickel	Ad20	50	10	15	NO	confined
Ni-Short	Nickel	Ad20	50	5	15	NO	confined
Ni-DC	Nickel	Ad22	50	10	15	YES	confined
Ni-free	Nickel	Ad22	50	10	15	YES	free

Table 2.1: Samples irradiated in this work's data taking. See text for detailed explanation of quantities. Note that length and alumina thickness are estimated from deposition time, and have not yet been directly measured, therefore a difference up to 2 μm from nominal values is possible.

Where the listed parameters are:

- **NWs metal:** different metals can be used for electrodeposition. Most samples were filled with nickel nanowires, but a group of three samples with different metals (Ni-thin, Co-Thin, Fe-Thin) were realized with very similar parameter except filling metal, to compare performances of nickel, iron and cobalt NWs.

- **Support label:** The (arbitrary) label assigned to the physical aluminum substrate used for a sample. It is of little interest for this thesis purpose, except to note that some samples were actually different regions in the same physical sample.

- **NWs diameter:** As described in section 1.1.1, nanowires of different diameters can be produced by using different electrolytes during anodization. In this case, 20 nm

diameter NWs (i.e. "Thin" samples) were obtained via sulphuric acid anodization, while 50 nm NWs via oxalic acid anodization.

- **NWs length:** Nanowires of different length can be obtained adjusting deposition times. Nanowires of different length have been fabricated either on the same physical support, by raising it partly out of the solution during electrodeposition, , or on a thicker alumina matrix. In the first case, the two resulting regions are referred to as Ni-Long and Ni-Short.

- **Metal contact**: The base of nanowires can be in direct contact with the aluminum substrate, or separated by an insulating oxide layer few tens of nm thick. Most samples have been produced without electrical contact (via AC deposition), but one sample (Ni-DC) has been produced via DC deposition, so its NWs are directly in contact with the aluminum substrate.

- **NW confinement**: For most samples, the alumina template is left intact after NWs deposition, so NWs are "confined" in the alumina. For the DC sample, the alumina layer was dissolved by chemical attack in a limited region, leaving the nanowires "freestanding". This region is referred to as "Ni-Free". This could be done only to a sample with contacted NWs, since non contacted NWs collapse without support from the template.

As can be seen, quite a large range of parameters was included in these samples. Focus of this thesis' work was to use morphological analysis and measurements from online detectors to find out which samples yielded best results, aiming at obtaining a plasma as hot and dense as possible.

2.2 Experimental setup

The samples (which will be called "targets" in this section) were irradiated by a pulsed laser at an INFN facility (Laboratori Nazionali del Sud) in Catania in April 2016. Data from various detectors were collected during irradiation and later, once the targets were returned to Bologna , craters were analysed at SEM and optical microscopes. In the following subsection, the laser setup and the detectors will be described.

2.2.1 Laser setup

Targets were placed inside a vacuum chamber, held in position by a metal target holder which can be moved with great accuracy, providing the desired spacing between shots. The elements of the irradiation setup (not considering the detectors) are:

- **Laser:** a Q-switched solid state Nd-YAG laser has been used for irradiation. It fires in 6 ns long pulses, with a maximum rate of 10 Hz. It emits light in the near infrared, at 1064 nm wavelength. Each pulse carries a nominal maximum energy of 2,2 joule. The laser beam is generated outside the chamber and has a diameter of 2 cm, so before reaching the target it crosses a transparent window and a convergent lens.

- **Vacuum chamber:** lens, target and detectors were all contained in a 800 mm diameter cylindrical vacuum chamber, inside which a pressure of 10^{-4} torr was obtained.

- **Focusing lens:** a fused silica plano-convex lens with focal length 67 mm focuses the beam on the target. The incoming laser beam makes a very small angle (few degrees) with the focal axis of the lens, in order to avoid that light from the target is focused back towards the laser. Between the lens and the target is a thin sheet of transparent mylar, to avoid condensation of ablated material on the lens. The laser beam should shrink to about 100 μm diameter on the focal spot. As will be discussed later, proper laser focusing was found to be a key parameter to get reliable data.

- **Target holder:** a metal target holder has been employed to keep the target in position, and to connect it to the movimentation system. Since preliminary data suggested a problem with lack of planarity of the target holder, a new one was produced at the INFN Bologna workshop and used for the data taking.

- **Movimentation system:** The target holder is connected to a movimentation system which can move in three dimensions. It is used first to change the distance of the target from the lens (z axis movement) in order to find the focus position, and then to shift to target in the x-y plane between shots. It allows x-y-z movements with 1 μm increments, in a 26 mm range. The normal to the target is kept at an angle of 30 degrees relative to the incoming beam, so that planarly reflected light does not go back toward the laser.

Image 2.2 shows the inside of the vacuum chamber.

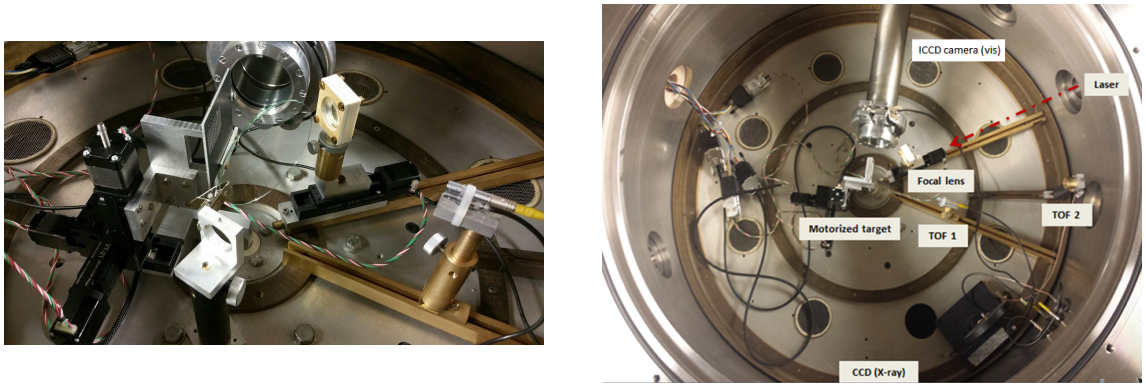

Figure 2.2: Vacuum chamber at LENS laboratory. The lens can be seen in its white plastic case, along the laser beam path. On the left, the target can be seen in its holder. On the right, a top view of the camber can be seen, with the different detectors and instruments labelled.

2.2.2 Online detectors

Several detectors are contained inside the chamber and are used to gather data during the event. Data from these detectors are used both for real time feedback (for example, ToF signal was found to be useful for focusing) and for offline analysis.

A single timing signal is generated for all detectors and for the laser itself, so that time can be measured from the beginning of the laser pulse.

The available detectors are:

- **ToF detectors:** time-of-flight measurements allow to measure the velocity distribution of ions escaped from the plasma. For this measurement, LEMO connectors at negative voltage have been used as ion collectors. Signal from the LEMO was amplified outside the chamber and sent to a digital oscilloscope. Data from ToF were both displayed in real time and saved.

  Two groups of three ion collectors have been placed inside the chamber, one approximately 15 cm from the target (ToF near) and one approximately 30 cm (ToF far) - see figure 2.2. Both groups are almost collinear with the laser beam.

  ToF data were found to be also reliable for focusing feedback.

- **CCD camera:** an Andor DY920P model back-illuminated CCD camera provided data on X-rays emission from the plasma. To gather information about X-rays energy, a pinhole mask was applied to the camera, with foils of aluminum of different thickness (in a 3 to 17 μm range) in front of each hole. Comparing the flux through each pinhole allowed a rough estimate of the energetic emission spectrum of the plasma in the few keV range.

  Data from the CCD camera are integrated over ten μs - a much longer time than

the lifetime of the plasma - and thus yelds no information about the time evolution of the plasma.

- **ICCD camera:** an Intensified CCD camera, positioned 23 cm from the target at low incident angle, has been used to gather time-resolved data about the 2D expansion of the plasma plume. It records the visible radiation coming from the plasma in the wavelength range 200–900 nm.

2.2.3 Offline imaging

After laser irradiation, targets were sent (or brought) back to INFN lab of the Physics and Astronomy Department of the University Bologna, where the morphology and composition of craters could be studied. Part of this thesis work consisted in systematically collecting and analizing crater data with the optical microscope, further analizing structures of interest with a scanning electron microscope (SEM).

The instruments employed for imaging were:

Optical microscope: a Huvitz HDS-5800 optical microscope has been used to image craters and other features on the targets. It offers a range of magnification between 240x and 5800x, and it allows target movement with 2 μm precision in the x-y plane (parallel to target surface) and 100 nm precision in the z axis (normal to surface).

The microscope has very useful image manipulation capabilities: most important to us were the ability to stitch together several images to produce a composite image of a large surface, and the ability to quickly take several (dozens or hundreds) of images at different Z position, determine the focal plane from each, and generate a composite 3D-model of a surface. See figure 2.3 for examples of the generated models.

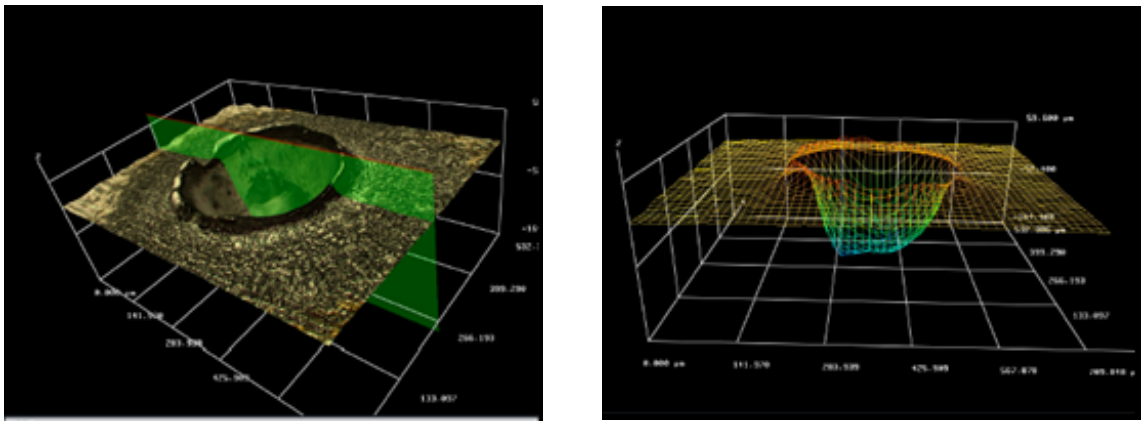

Figure 2.3: 3D model in colour view (left) and mesh view (right) generated by the optical microscope. This kind of models allow geometical measurement with μm precision

The capability to easily build 3D models of laser craters and measure their geometrical parameter (such as ablated volume and depth) was hugely useful for this work, since it allowed to observe qualitatively and compare quantitatively the craters formed on different targets. Along with X-ray measurement, images from the optical microscope were so far the most useful to discriminate the properties of different targets.

Resolution of 3D models created by the microscope is limited by optical considerations, capabilities of the model-building software and artifacts. This contributions will be discussed more in depth in the next chapter, but as a first consideration, these models were found to be accurate within few μm when comparison with other measurements was possible.

No optical microscope could possibily resolve single nanowires (those used for this study were all below 100 nm in diameter), so images and models taken with this microscope are useful down to the micro level, but SEM observation was required to directly observe the nanoscale effects of irradiation.

The microscope software allowed for collection and simple statistical analysis of geometrical data, and was extensively used for this thesis work.

SEM a Philips 515 Scanning Electron Microscope, located at the INFN microscopy laboratory in Bologna, was also used to observe the targets. It can reach x40 000 magnification, but since targets did not conduct well (alumina is an insulator), sharp images could rarely be obtained beyond x10 000 due to charge accumulation. While this microscope model was not originally built for digital conversion of images, it was upgraded in past years to allow acquisition and saving of digital images.

This electron microscope has two operating modes (shown in fig 2.4)

- **Backscattered electrons imaging:** this mode is used for most imaging purposes, since it yields high resolution images up to tens of thousands of magnifications. It is very sensitive to charge accumulations, which led to some difficulties since the alumina layer on the targets is non conductive.

- **Microanalysis:** this mode yields no image, but analyzes the X-rays emissions of the target in response to the electron flux. Since electrons usually carried a 15 keV energy, K line emission is possible, thus allowing the discrimination of elements in the target. This mode was very useful to distinguish the metal from the aluminum substrate from that of the NWs.

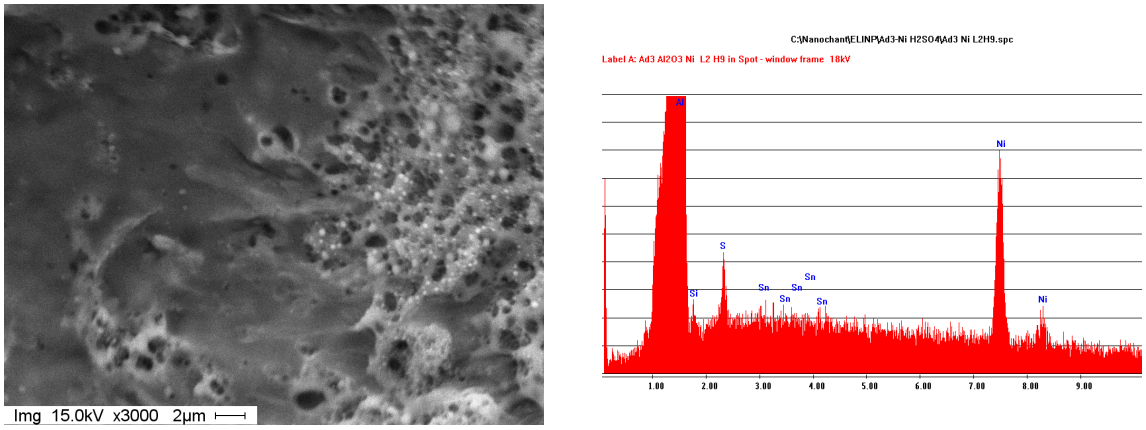

Figure 2.4: Comparison of SEM operating modes. Left: SEM backscattered electrons image of the bottom of a crater. Nanoscale features (the light coloured "bubbles" on the right are likely to be partly molten NWs) can be clearly resolved. This is very valuable to check the quality of targets, and to understand the effects of irradiation on the nanoscale. Right: Microanalysis measurement from the same region. X-rays frequency peaks are used to identify elements. As can be expected, aluminum and nickel are the most prominent peaks, followed by sulphur (leftover from sulphuric acid anodization)

SEM measurements have been crucial for several steps of this work:

- **Parameter control of targets:** while alumina thickness and NWs height can be estimated from anodization and electrodeposition time, electron microscopy allows to directly image the nanostructures and measure their geometrical parameters. Since the targets need to be broken to see the NWs channels, this analysis was performed on the control targets instead of the actual targets.

  NWs of greater diameter (produced by oxalic acid anodization) could directly be observed within the channels, while those of smaller diameter (produced by sulphuric acid anodization) were too small, and were measured performing microanalysis at various heights of the alumina layer to test the presence of the NW metal.

- **Qualitative observation of craters:** comparison between optical and SEM images has been particularly useful, since SEM images allow to understand what kind of nanostructural modifications cause a given colour or texture.

2.3 Improvements to setup

Before this work's data taking, preliminary targets had already been irradiated. Part of this thesis work was performing morphological analysis on the resulting craters. Information from these targets was used to choose which kind of targets to fabricate for this work's data taking, and how to improve the experimental setup to get best performances. The most important change was related to the focusing of laser light on the target.

Analysis of the data collected in the first phase led to further modification of the experimental setup, some to solve issues and some to improve the performance of detectors (single photon counting) which will be useful in future data takings.

2.3.1 Laser focusing issues

During preliminary data takings, the laser beam had been focused with a simple method: a line of craters was shot on the target, moving it also on the Z axis (perpendicular to its surface) between each shot. The resulting craters were observed optically, and that of smallest radius selected. Z positioning of the target was then moved to the value corresponding to the selected crater.

During the morphological analysis of preliminary targets, several issues were found which were suspected to be focus-related:

- Craters along the same row were very similar in depth and geometry, even down to very specific structures, but different rows were considerably different.
- Some craters showed two separate points of maximum depth. This effect was most evident in the most shallow craters.
- Craters were often ringed by elliptical lines of damaged but not completely removed alumina, in a very specific pattern.
- Most craters showed a peculiar structure: a very long, shallow area of burned alumina and molten aluminum which begun from the crater and extended for several times it diameter (hundreds of μm) along the direction of the laser's beam momentum component parallel to the surface. No description of such a feature, which was dubbed "the valley", was found in literature.

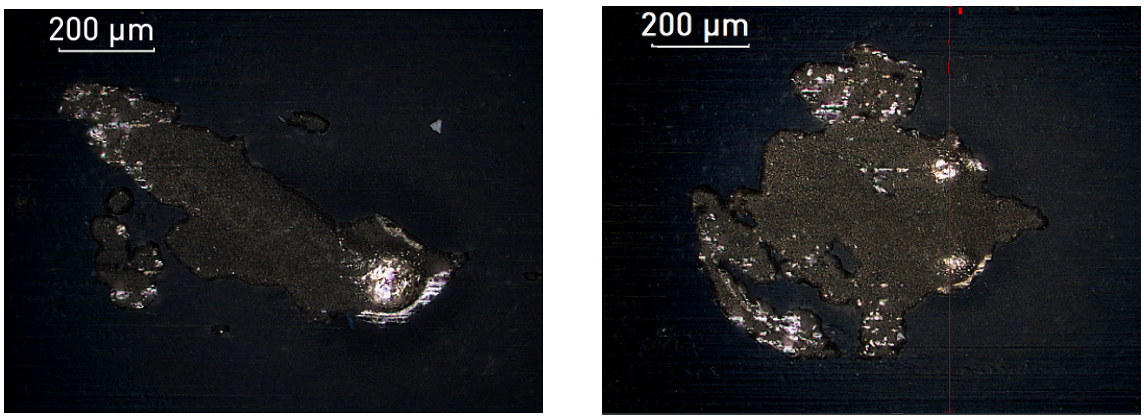

Figure 2.5: Irregularly shaped craters due to suboptimal focusing. On the left, the wide and shallow ablation region dubbed "valley". On the right, a crater with two clearly different points of maximum depth (visible as bright spots due to high reflectivity)

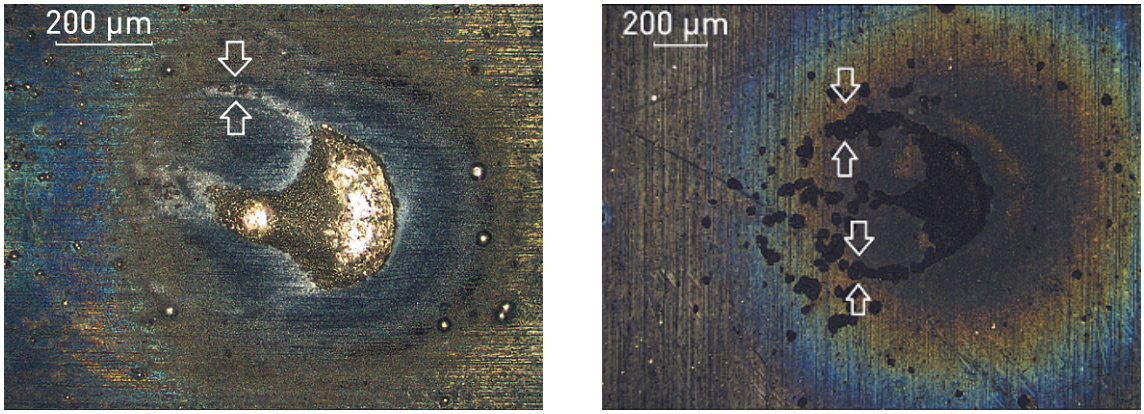

Figure 2.6: The elliptic lines pattern typical of out of focus craters. They were likely due to the spatial intensity distibution of the out-of-focus laser beam

In image 2.6 the described features can be seen. The extreme similarity between shots on the same row (but not in the same column) led to think that the difference between rows could be due to difference in the beam focusing, since the target should have the same regularity through rows and columns.

Since the target, and not the lens, is actually moved between shots, the problem was likely tied to the movimentation plane not being perfectly normal to the target's surface. This could be due to non-planarity of the target holder, the target not being tightly secured to the target holder, or the movimentation system not being perfectly aligned with the target holder.

Elliptic lines and double minima were suspected to be caused by the intensity distribution of the out-of-focus laser.

No clear explanation of the valley formation mechanism has been found so far, but it was very likely caused by focusing issues, since it has no longer been observed with the new focusing method.

To address this focusing issues, a new target holder (which can be seen in figure 2.2 with metal strips to press down the target was built, and a new focusing algorithm employed, which works as follows:

- Four different block of 3x3 or 3x4 shots are fired at the corners of the target surface. For each block, the Z position of the target is gradually changed, usually in 100 μm steps.

- For each shot, Z position of the target and the time of the peak in ToF-far signal is recorded. Shots with the shortest time to peak (i.e. most energetic ions) were considered to be the best focused ones. See figure 2.7 for a typical result.

- The area between focus blocks is irradiated. For each shot, a Z correction is added so that the focus position moves on the plane defined by the four in-focus shots.

With this algorithm, it was soon found that the best focus position, with little difference between ToF results, is about 200 microns deep. Moving away from the best focus, ToF times steeply increase. This method is very robust, because it works independently of the exact cause of non planarity.

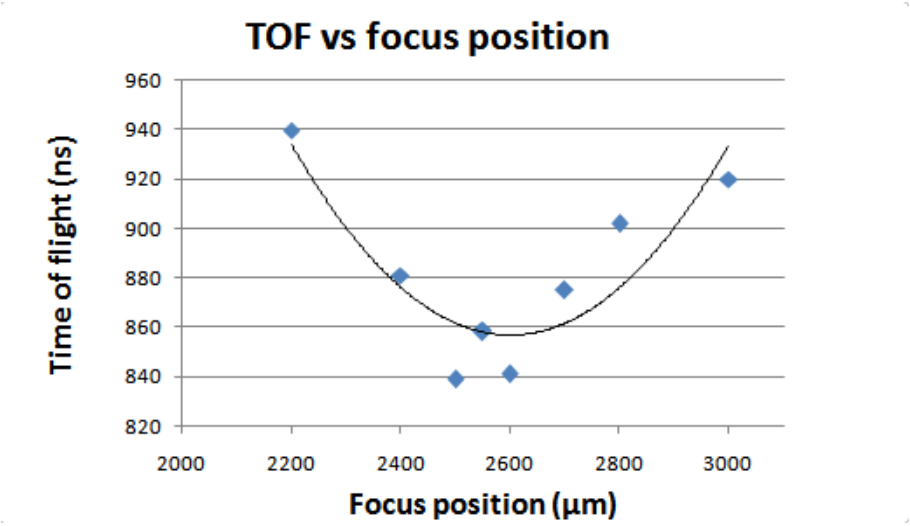

Figure 2.7: ToF time-to-peak measurement vs focus position. There is little difference in ToF time for values near the minimum, but there is a steep increase beyond a 100 μm distance from the best focus position.

Craters fired with the new target holder and the new focus algorithm have no apparent issue of row-by-row consistent irregularities, do not show the "valley" structure, and are considerably deeper (one and half time as deep) than the deepest of craters in preliminary data. Also regularity of craters' shape has greatly increased.

All this considered, it appears that non-optimal and inconsistent focus was a major issues in all preliminary data, and while their broad trends - such as the ten-fold increase in X-ray flux from Al-Bulk to nanostructured targets - have been confirmed, more detailed observations (such as any comparison between different nanostructured targets) are unreliable and have not been included in this work's analysis.

2.3.2 Single photon counting

While the ICCD camera gives useful information about the X-ray flux, it does not directly measure the energy of photons. To gain some energy sensitivity, the previously described pinhole mask with aluminum absorbers has been employed. Absorption coefficient of aluminum decreases with photon energy, so thicker absorbers transmit a higher proportion of hard X-ray compared to thin ones. This allows some comparison of X-ray spectra from different targets.

In principle, comparison between flux through different absorbers could give quantitative information on photons energy. Unfortunately, the X-ray spectrum was found

to be dominated by soft (< 3 keV) photons. Trying to calculate their energy with the absorber comparison would be extremely difficult and imprecise, since even very small uncertainties on absorber thickness and stochastic fluctuations on fluxes would greatly impact the calculation.

So, a different method was employed: one of the pinholes was covered by a thick aluminum foil (50 μm), so that for each event, no more than a single photon is likely to to hit a pixel. The appropriate thickness was found simply by with increasing thickness of the absorber. The so-called "single photon regime" is obtained when the number of hits per event is smaller than about 1% the number of pixels. .

Since the charge produced by a single photon in a CCD detector is directly proportional to its energy, this technique allows us to measure the energy of photons from the plasma. In future data takings, the whole CCD detector will be dedicated to single photon counting, allowing a direct measure of the plasma's emission spectra (which need to be deconvoluted from the CCD quantum efficiency). X-ray spectra can be very useful to calculate plasma temperature.

Chapter 3

Data and analysis

In this chapter, data collected for this work will be presented. In the first section, data from the morphological analysis of craters, in the form of optical images, SEM images and geometric measurements, will be presented, along with an explanation of the criteria used for crater selection and uncertainty extimation. The second section will deal with X-ray flux data from the CCD camera.

3.1 Morphological analysis

Most of the morphological analysis of craters was conducted with the optical microscope (described in section 2.2.3), thanks to its capability to create 3D models of the craters and perform geometrical measurements. The aim of this work is to use the collected data to find which materials are more suitable to produce a hot and dense plasma.

However, the relationship between crater morphology and plasma parameters is not immediate, so it is not trivial to decide which features are indicative of a "good" plasma and which are not. Since the advantage of nanostructured materials compared to bulk aluminum lies in the volumetric heating of matter, it was decided to simply measure depth and volume of the craters. Later in this section, it will be explained how this quantities were measured, discussing the limitations in the chosen approach and the calculation of uncertainty.

One more choice to be made in the process of data collection was deciding which craters to include in the analysis. Due to laser focusing and other setup issues, some craters were irregular or very shallow. The criteria for crater acceptance or rejection will also be discussed in this section.

Finally, at the end of this section the morphological data (aggregated by target) will be presented.

3.1.1 Craters description

Most observed craters have a sharp circular shape, with diameters ranging between 150 and 180 μm. It should be noted that this is considerably more than the laser spot size (which is approximately 100 μm in diameter).

A crater's depth (measured at the deepest point) is, in most cases, greater than its radius but a little smaller than its diameter - the exception being Al-Bulk, which has greater radius than depth. The crater bottom is hemispherical in general shape, but often displays a structure called "channel", (see figure 3.1) a straight narrow indentation, resembling a knife cut, which begins at the centre of the crater and points downward, toward the same direction as the parallel component of the incoming laser beam.

This structure is definitely related to the inclination of the incoming laser beam, but surprisingly it is usually much more narrow (few tens of μm) than the spot size of the beam, so it seems unlikely to be a direct consequence of the spatial distribution of laser intensity. While its exact origin is unsure, optical observation and SEM imaging led to hypotize that it originates from a rapid cooling of convection patterns at the crater bottom.

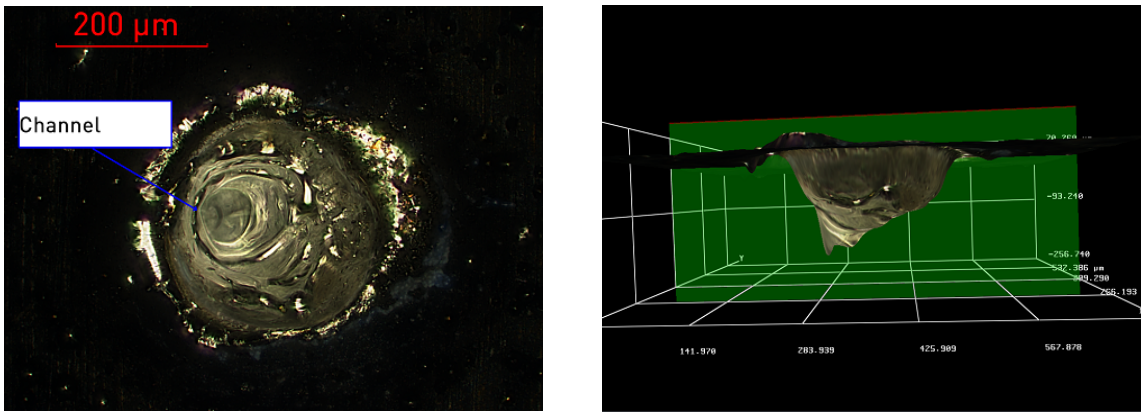

Figure 3.1: The channel structure, common in craters of all targets, seen from top (left) and side (right). As can be seen, the channel is a strongly asymmetric deep indentation in a mostly hemispheric crater. In this image, the laser beam arrived from the right.

Considering the surface outside the craters, different targets show different features - with different NWs material seeming to be a key factor.

Features observed next to crater's rim, for different targets:

- **Bulk-aluminum** shows a slight (less than 5 μm) swelling around the crater, likely due to thermal modifications during irradiation [22]. Outside the crater, there is often sign of surface melting (see figure 3.2) in a 100 to 200 μm radius.

- **Targets with nickel NWs** often show "peeled off" alumina around the crater (see fig 3.2), revealing intact aluminum. As can be seen in figure 3.2, the oxide layer

breaks off along geometric lines. This is probably due to rapid thermal expansion of the material below, which causes rupturing of the alumina layer.

- **Targets with iron NWs** show a different feature: around the crater, alumina undergoes a radical modification, becoming white and foam-like in appearance (see fig 3.3). They are also the craters with smaller radius.

- **Targets with cobalt NWs** usually show no evident modification of alumina outside the crater (see fig 3.3), but differently from all other targets, some of them (approximately 25%) show a crater ridge, about 10 to 50 μm above the alumina surface. This, along with the presence of peculiar "debris projections" and "pits", which will be described later, seems to imply that molten matter movement is more important in Co targets than in other kinds.

- **"Free" nanowires** (obtained in DC targets, after alumina removal) form craters of comparatively small (150-170 μm) diameter, but depth comparable to those in confined NWs targets. Their edges are difficult to observe with an optical microscope, since there is not as great a reflectivity difference as in confined targets (see fig 3.4). They are much easier to distinguish in SEM images: matter inside craters is visibly molten, and a peculiar pattern of ball-like structures surrounds the crater. Lack of conduction through alumina is thought to limit the lateral expansion of craters.

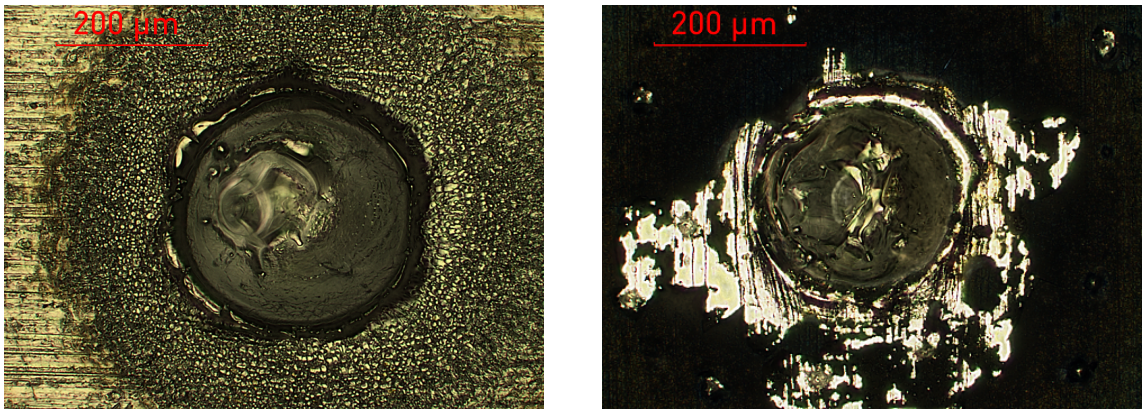

Figure 3.2: **Left:** Typical crater in bulk-aluminum. The shape is very regular, and modification of the surface, probably due to melting, can be seen hundreds of μm from the crater's edge. **Right:** Typical crater in target with Ni NWs. As can be seen, the alumina layer is "peeled off" around the crater, revealing intact aluminum below (lamination lines, vertical in this image, can be noted). The surface appears very dark due to the contrast with higly reflective aluminum.

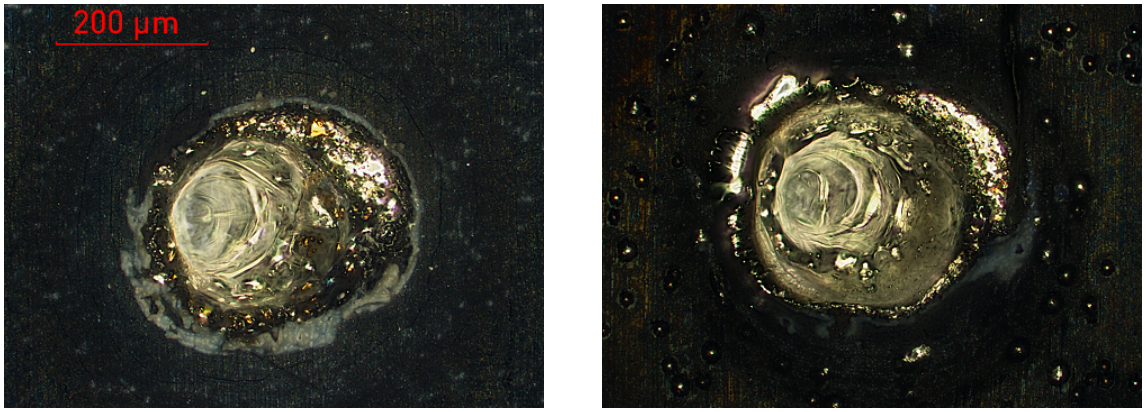

Figure 3.3: **left:** Typical crater in target with Fe NWs. The most striking feature of these craters is the formation of a white "crust", foam-like in appearance, between the crater and the comparatively intact alumina around it. **Right:** Typical crater in target with cobalt NWs. The reflective regions around the crater are raised 20-50 μm above the target surface, forming a ridge.

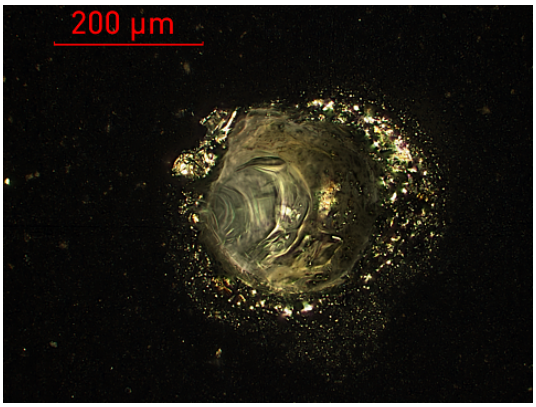

Figure 3.4: Typical crater in target with freestanding nichel NWs. Craters in this target are comparatively small in radius, and surrounded by a small area of molten surface

Surface modifications: the surface of irradiated targets undergoes several modifications after laser irradiation. While some can be seen with an optical microscope, comparison with SEM often offers useful insight.

Target surface modifications often affect a wide area - even a millimeter long. Therefore,adjacent shots must be spaced at least 2 mm to avoid ablation on material already modified.

The different kind of surface modifications found in irradiated targets are:

- **Foam-like material:** at the bottom of craters, usually "clean" bulk aluminum metal can be found. But at the edges, and sometimes at the bottom, residual matter from alumina, nanowires and aluminum mix in a foam-like material (see fig 3.5), with collapsed and partly molten NWs forming "bubbles" up to 200 nm in size which appear bright at SEM analysis.

- **Shredded alumina:** while alumina near the crater (tens of μm from the rim) is much less reflective than the aluminum in the crater and looks intact at first sight, it can be noted it gets brown hue. SEM imaging reveals that alumina in this region is heavily damaged (see fig 3.5), with the ordered channel structure completely lost. Measuring the extent of shredded alumina could be useful in future analysis to understand how far heat propagates from the crater.

- **Coloured alumina:** farther from the crater (hundreds of μm to millimeters), the most evident modification is a change in surface colour, which gains a yellow hue (near to the crater) and then a blue one (farther from the crater). This coloured halo can be seen quite clearly (see fig 3.6) when using a point light source, but disappear completely with diffuse illumination. This led to hypotize that colours are due to interference effects - possibly caused by partial melting of NWs inside the pores. A different hypothesis is that colours are due to thermal combination of alumina with residual gas in the chamber, i.e. mainly nitrogen and oxygen. In future, SEM microanalysis could be used to test these hypotheses.

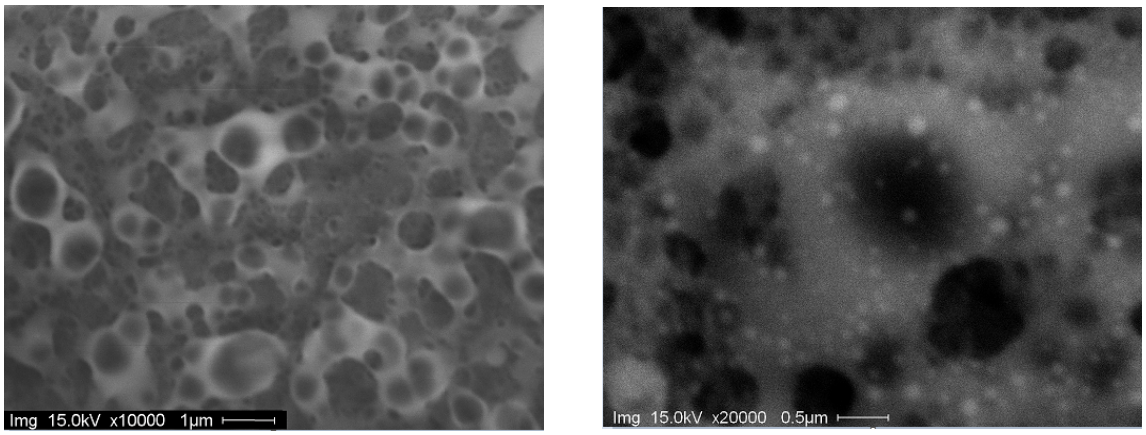

Figure 3.5: left: shredded alumina few tens of μm from a crater in a preliminary target. The ordered structured is completely lost. NWs are no longer visible, likely due to the swelling of the alumina surface during the shredding process. This damage is likely caused by shockwave propagation in the target. Right: foam-like material at th bottom of an out of focus crater. Residual of NWs are still visible as brigh bubbles in the alumina.

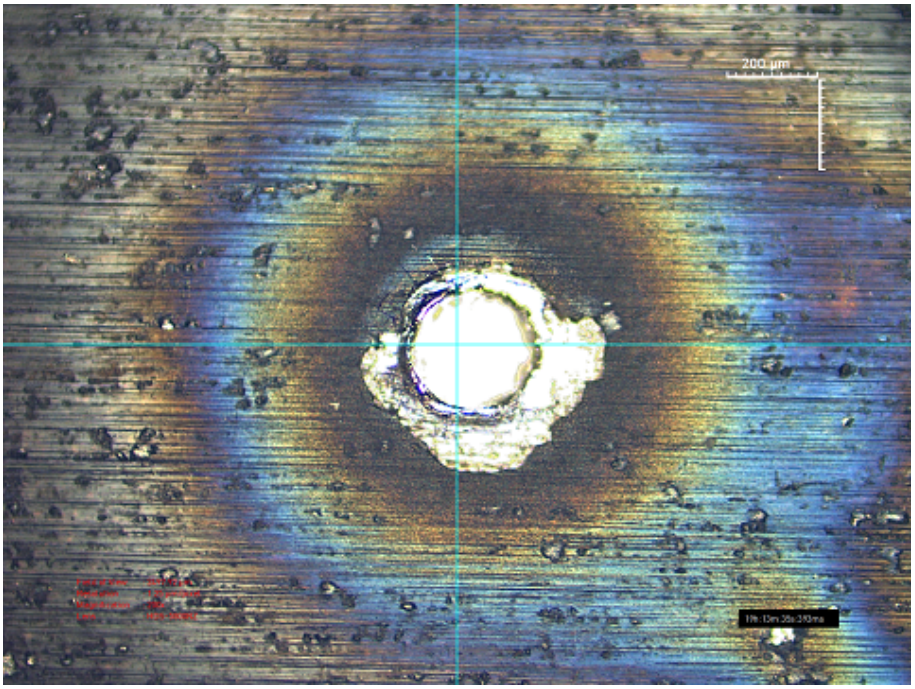

Figure 3.6: Surface modifications of alumina, seen with point like white light source (bright field). Near the peeled off zone, alumina is brownish and rough in appearance: this is the "shredded alumina" region, where the ordered structure is lost. Farther from the crater, alumina is mostly intact (lamination lines are still visible), but acquires coloured haloes. Different targets show slightly different colour patterns, but shorter wavelength colours are always on the outside.

Some other peculiar features were found in specific targets. Although no statistical analysis was performed on them, their presence (or absence in different targets) can shed light on the physical processes which occur during irradiation.

Debris projection: one interesting feature was found in several craters, most of them in the target with cobalt nanowires: a rough circle of fused metal, above the surface level, tangent to the crater (see figure 3.7). In most cases, these debris are tangent to the crater along the direction of the component of the laser beam parallel to the surface, but sometimes the debris forms towards the laser, sometimes opposite it.

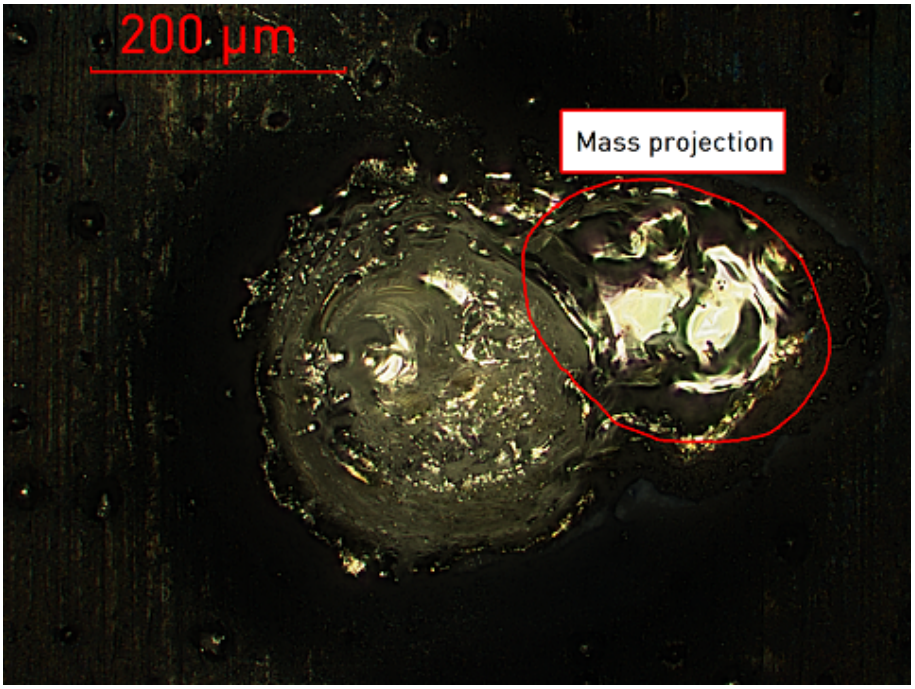

Figure 3.7: Debris (mass) projection in target Co-Thin. It can be seen as a smooth and highly reflective area near the main crater. In this case, the molten material is in the direction of the incoming laser beam (right).

Likely, this debris is formed by matter flow at liquid phase. Together with other features, this might indicate a more important liquid phase in targets with Co NWs compared to other materials.

Pits: several targets show circular "pits", a few μm wide, pock marking the alumina surface around the crater (see fig 3.8). Most of them are too small to reliably measure their depth with the optical microscope due to diffraction, but the widest ones seem to be as deep as the alumina layer. SEM analysis shows the bottom of the pits is conductive, therefore it seems these pits reach the aluminum under the oxide.

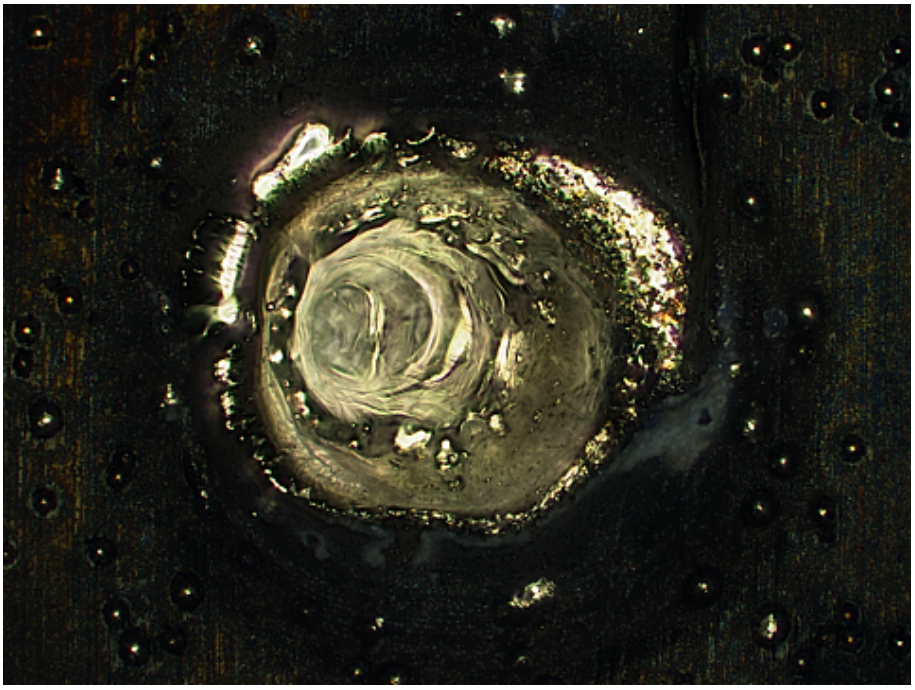

Figure 3.8: Pits in target with cobalt NWs - the small circular marks which surround the craters. The high reflectivity at the centre of pits is likely from aluminum substrate, meaning the whole alumina layer has been removed. Pits are likely due to laser light reflected by the plasma.

At least some pits can be found in all targets except the bulk-aluminum one. They have a peculiar spatial distribution: they are absent near craters, become more frequent near a specific radius, and then become less frequent again. This peculiarity led to think they are due to reflected laser light, possibly scattered by the expanding plasma plume. While they have not been analyzed in detail yet, should the plasma scatter hypothesis be confirmed pits density could provide useful data on plasma development.

3.1.2 Morphological measurements

In this subsection, morphological data systematically collected on the craters will be presented, explaining the criteria used to choose which crater were included in the analysis, and how measurements have been performed.

Measurement process: the optical microscope used for this work allows several kind of measurements on the 3D models it creates, including linear, superficial and volumetric quantities. It is not trivial to decide which geometrical parameters are indicative of more energy absorption. Also, due to the structure of craters, some measurements could be reliably performed with low uncertainty, while others required arbitrary decisions or led to high uncertainties.

After comparison of several kinds of measurement strategies, only two parameters

were included in the final analysis: crater depth and volume. They have been measured in the following way:

- **depth**: first, a line is chosen along which the crater's depth profile will be measured. It was decided to choose a line parallel to the laser beam direction and passing through the point of maximum depth. Since surface outside the crater is quite flat (within two μm) for all considered targets, depth is simply calculated as the height difference between a point well outside the crater - to exclude local swelling and other near-crater features - and the deepest point of the crater.

- **Volume**: to measure volume, it is necessary to define a 2D measurement region, and a reference level. Empty volume will be calculated below the reference level, and only in the selected region. Reference level is taken at the surface. At first, the 2D region was defined as a closed geometric line following the rim of the crater, but it was found that simply selecting a circle a few tens of μm wider than the crater gave results within 1% of the point-by-point defined area, so a circle was used for simplicity and to avoid ambiguities in the exact criteria for crater edge definition.

  It was also decided that empty volume due to peeled-off alumina should be included in volume the measurement.

Two more parameters were initially considered viable for analysis: crater diameter and crater curvature radius. Crater diameter was excluded due to ambiguities: features present in some targets (raised crater rim, peeeled off alumina) made difficult to choose criteria for measurements, incurring the risk of misleading systematic differences between targets. Curvature radius was found to have large uncertainty and was difficult to measure in targets exhibiting channel structure.

Craters choice: despite appropriate tuning of the experimental setup, it was soon evident that not all craters could be part of the analysis. For example, the laser was subject to occasional glitches, focusing problems occurred during the data taking phase, and some craters were clearly different from the others.

So, a policy had to be set for the choice of which craters should be included in the analysis, in order to avoid including data contaminated by setup problems.

So, the criteria for craters selection were:

- **Focusing:** all craters outside focus blocks (fired with focus correction algorithm, as described in 2.3.1) were considered to be in focus. Rejecting all data from focus blocks, though, would have been wasteful. So, for focus blocks craters, data from ToF were considered: as can be seen in figure 3.9 the Z scan usually finds a minimum

ToF position, and away from it signal increases in an approximately parabolic way - therefore, shots near the best focus position have very little difference in ToF timing, but it increases steeply for farther shots.

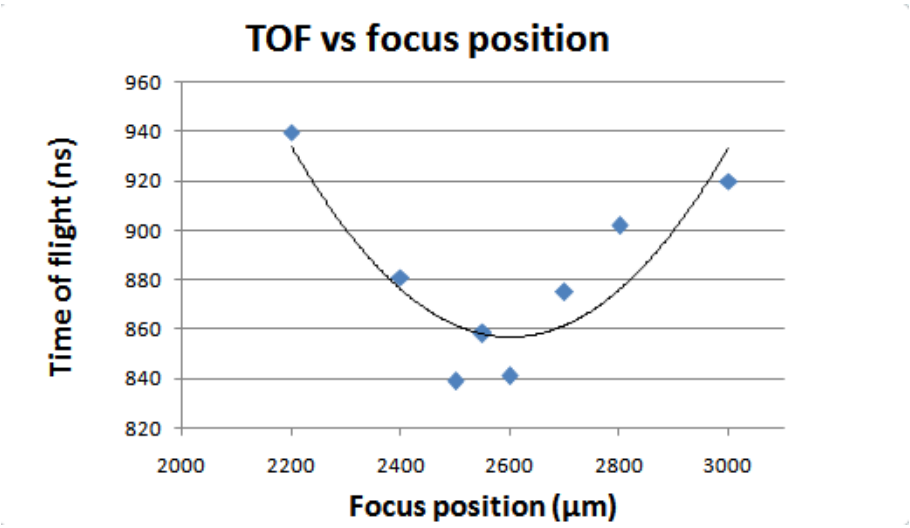

Figure 3.9: ToF time vs focus position. There is very little difference within the ToF results for data points near the minimum, so craters from focus blocks within 100 μm from the best focus position were included in the analysis.

Shots within 100 μm from best focus position were considered in focus. As a validation of this choice, average depth from focus block craters was compared to average focus-corrected craters, and no statistically significant difference was found for any target.

- **Regularity**: the majority of craters have a very regular circular shape. Some (see fig 3.10) were instead very irregular, with deep cracks and regions of peeled-off alumina - and intermediate configurations were very rarely found. Since irregular shape was usually associated with shallow depth, it is strongly suspected that irregular craters are due to laser misfires. Due to this, evidently non-circular craters have been excluded from analysis.

  Some craters had to be excluded due to suboptimal setup conditions during data taking (for example, ablated material caused opacization of the mylar sheet used to protect the beam focusing lens, causing diffusion of the laser light until mylar was changed) or laser misfire.

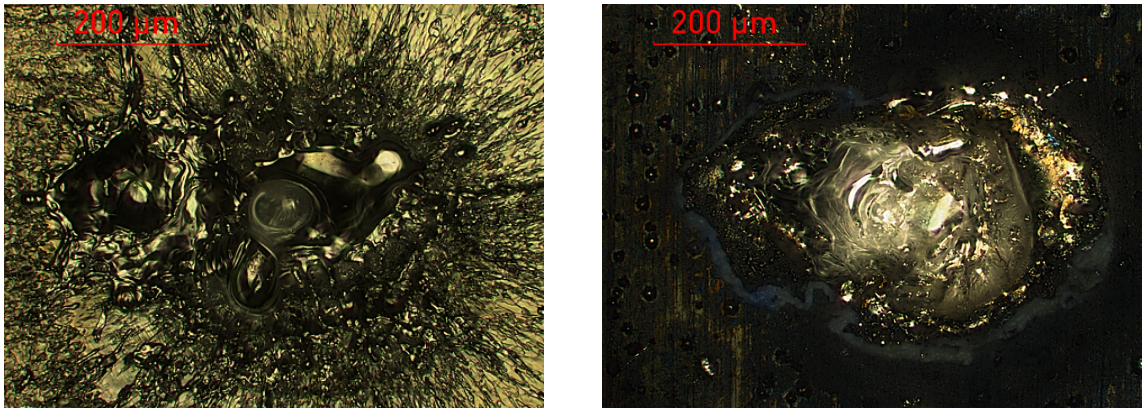

Figure 3.10: Out of focus craters in Al-Bulk (left) and Co-Thin (right) targets. These craters are shallow and irregular in shape

All this considered, table 3.1 shows the number of craters included in the analysis for each target. For most targets, 20 to 30 valid craters were available. Unfortunately, the statistic is lower for Ni-Long target due to setup problems during irradiation, and for Ni-free due to a low total number of craters (alumina was removed only for few rows of shots) and laser glitches.

Number of analyzed craters		
Target	Total craters	Valid craters
Al-Bulk	55	23
Ni-Thin	53	19
Co-Thin	57	28
Fe-Thin	57	31
Ni-Long	34	7
Ni-Short	34	23
Ni-DC	36	23
Ni-Free	15	8

Table 3.1: Total number of craters (including the ones used for Z scan) and number of craters included in the analysis for each target. For most targets, 20 to 30 valid craters were found, but targets Ni-Long and Ni-Free were affected by setup issues, and less than 10 usable craters were found

3.1.3 Uncertainties and statistics

Measurement of craters' depth and volume found significantly different values within each target. To account for this differences and provide accurate mean and uncertainty

values, two sources of fluctuations must be taken into account: actual differences in craters within a target, and uncertainties on depth or volume measurement. In addiction to this statistical fluctuations, possible systematic errors will be discussed, and the steps taken to minimize them described.

Setup uncertainties: during the data taking, not all experimental variables could be perfectly controlled. While a huge number of experimental parameters could influence the resulting crater for each shot, the most important sources of uncertainty are thought to be the following:

- **Laser energy:** in the current setup, there is no shot-by-shot control of laser intensity. Since energy calibration is performed measuring the total energy delivered by a high number of shots, the variance of energy between shots is currently unknown, and could be an important contribution to morphological fluctuations between different events.

- **Laser focusing:** while the new focusing algorithm greatly improved performance and consistency of the laser setup, small focusing differences between lines could still be present - for example, if the target surface is not perfectly planar, a linear Z correction is less effective. Since no significant difference has been found between different regions of the same target, focus effects cannot be too large, but they could still be a source of uncertainty.

- **Target regularity:** even if the laser always delivered energy with exactly the same spatial and temporal distribution, the target surface could have local inhomogeneities. Pores length should be very regular and NWs length have a narrow distribution, with local difference between single NWs but not between different regions of the target, but some local fluctuations exist. Since a high number of NWs is included in the laser spot (order of 10^6), fluctuations in the number and shape of NWs should be small. Still, together with other target irregularities (metal grain, impurities, scratches and other minor damages, surface modifications due to previous shots) they probably contribute to craters' random fluctuations.

- **Intrinsic variability of the process:** even with optimal control over laser and target conditions, perfectly identical craters would not be expected. Plasma development involves many chaotic processes, and very small setup differences (or even intrinsic stochasticity of laser-matter interactions) could easily be amplified to different results.

Systematic measurement uncertainties: uncertainty on depth and volume measurement for each craters comes from different sources, some of which are quite difficult to estimate. Those considered most important are:

- **Resolution:** 3D models were built by software stitching of images captured at 2 μm step, so 1 μm is the effective vertical resolution of these measurement. For depth measurements, this means a $\sqrt{2}$ μm total uncertainty. As craters' depth ranges between 160 and 210 μm for all targets, resolution contribution to depth uncertainty is below one per cent. As for volume, resolution uncertainty has been considered to be vertical resolution times twice the measured region surface as a conservative estimate.

- **Surface definition:** Both depth and volume measurements require identification of a surface level outside the crater to be used as reference. While most targets' surfaces were very regular, sometimes swelling near the crater or surface irregularities made the definition of "surface level" outside the crater subject to some arbitrariety, especially for not perfectly planar craters. The extent of this uncertainty was estimated by measuring the difference from the highest and lowest point of the surface outside the crater, and considering that to be twice the standard deviation.

- **Deepest point identification:** The channel structure at the bottom of craters contributes very little to volume, but is important for depth measurement. Differences in illumination and geometrical orientation of the target lead to slightly different depth extimation by the 3D-building algorithm, due to difficulty of focusing the channel structure. By repeatedly scanning the same crater with different illumination and positioning, random fluctuaction due to this effect have been estimated to be $\approx 2\mu$m.

- **3D model building software**: Observation of surface scratches led to discover that the microscope's modelling algorithm does not work very well on thin grooves, and underestimates their depth. Since no other instrument was available to independently measure channel depth. This contributes a currently unknown systematic error to depth. To reduce it, target magnification and illumination have been chosen in such a way to produce as clear images as possible of the channel structure. In future, comparison with independent measurements could allow to evaluate this error.

Systematic measurement errors are reported in table 3.2.

Sources of systematic measurement uncertainties on depth and volume		
Source	σ depth (μm)	σ volume $(\mu m)^3 \cdot 10^5$
Vertical resolution	$\leq \sqrt{2}$	$\leq 0,2$
Surface identification	≤ 2	$\leq 0,1$
Deepest point identification	≤ 2	-
Total	3,2	0,22

Table 3.2: List of sources of statistical measurement uncertainty on morphological data. The listed values are to be considered maximum values, valid for all targets.

3.1.4 Morphological data

In the following table, depth and volume data from all the irradiated targets are presented. As previously explained, uncertainty is calculated as the standard deviation of the mean, while the systematic error is assumed to be the same for all targets and reported in table 3.2.

Morphological data for each target			
Target	Number of craters	Depth (μm)	Volume ($\mu m^3/10^6$)
Al-Bulk	23	139 ± 3	(3,67 ± 0,13)
Ni-Thin	19	160 ± 3	(3,99 ± 0,08)
Co-Thin	29	184 ± 3	(4,52 ± 0,05)
Fe-Thin	31	171 ± 4	(3,39 ± 0,09)
Ni-Long	7	203 ± 10	(5,32 ± 0,24)
Ni-Short	23	180 ± 4	(4,67 ± 0,05)
Ni-DC	23	189 ± 4	(4,20 ± 0,07)
Ni-Free	8	172 ± 10	(3,69 ± 0,24)

Table 3.3: Average depth and value of craters for each target.

As can be noted, difference between targets in terms of morphological data is usually several times larger than uncertainty. This means that, while there is some overlap between depth and volume of craters in different targets, their mean values are significantly different.

Interpretation of these data, along with that from X-rays, will be discussed in the next chapter.

3.2 Plasma analysis

During irradiation, X-rays, visible light and Time of Flight (ToF) measurements are performed. While their acquisition was not part of this work, X-rays data have been used together with morphological data to compare different targets. Another important feature of plasma is the energy of ions, which is collected by a Time of Flight system (ToF), as illustrated in chap. 2. A Python software has been developed to read, analyze and plot ToF data, even if, due to setup issues, ToF data have not been included in the analysis. However, the analysis of these data is still to be performed and will not be presented in this thesis.

In this section, a description of the X-ray and ToF data which have been collected will be given, and X-ray data will be presented target by target.

X-ray data: the CCD camera employed for X-ray data measurement has a pixelled screen, before which the previously described pinhole mask with aluminum absorbers of different thickness was applied. Note that while ten pinholes were present, three of them were found to have damaged absorbers, and were excluded from the analysis.

In figure 3.11, a typical resulting image can be seen. Each bright spot is beyond a different pinhole, with a different absorber. Each pixel in this image is coloured from black to white depending of the number of hits it counted on the pixel count, which is proportional to the collected charge. As can be easily seen, and should be expected, the flux through the thinnest absorbers is much greater than that through the thickest.

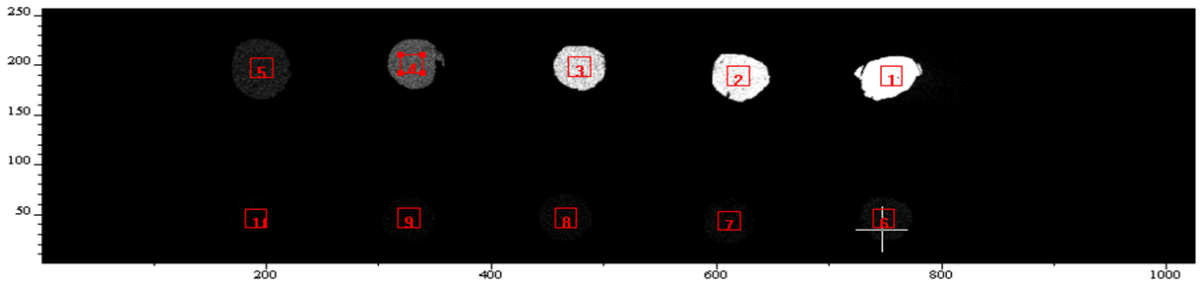

Figure 3.11: Output from the CCD camera for a single irradiation event. Pixels in this image represent direcly CCD pixels, with brighter colour representing a higher signal. Note the ten bright spot in the areas behind the then pinholes, with progressively darker spots for thicker aluminum absorbers. The red squares are the ROI (Regions Of Interest) selected for analysis.

From the global images, a Region Of Interest (ROI) must be set for each pinhole, inside which the pixels' counts are summed. ROIs can be seen as red squares in image 3.11

ROIs are all 100 x 100 pixels, and are manually chosen event-by-event so that they are centred on the ten spots. ROIs are completely contained in the x-ray "spot" corresponding to a pinhole, so any dependence on pinhole shape or size is avoided.

Before analysis, background - which is calculated pixel by pixel before each target's irradiation - must be subtracted. For the thickest absorbers, background can exceed signal, but since it is known with low uncertainty, its contribution to total uncertainty is small.

X-ray acquisition is integrated over a comparatively long (10 μs) time. Time resolved data from ion collectors and the visible light ICCD camera suggest the plasma does not last longer than a μs, so the whole event is integrated over.

While comparison between absorbers gives only a very rough sensitivity to X-rays energy, single-photon counting method will allow spectral analysis in future.

Target by target, X-ray data have been averaged over the same craters which were considered for morphological analysis.

Table 3.4 contains X-ray target-averaged data, for each of the seven considered absorbers. X-ray flux is measured as the average count per pixel of a given absorber's ROI.

Uncertainty is calculated as standard deviation of the mean, plus the contribution from background uncertainty.

X-ray flux vs absorbers of different thickness							
	Absorber (μm)						
-	5	6	8	9	12	15	17
Target	X-ray flux (count/pixel)*10^2						
Al-Bulk	22,9 ± 0,3	16,8 ± 0,2	8,5 ± 0,1	4,1 ± 0,1	2,3 ± 0,1	2,5 ± 0,1	1,2 ± 0,1
Ni-Thin	120 ± 11	90 ± 9	39 ± 4	12 ± 1,2	8,0 ± 0,8	7,8 ± 0,7	2,9 ± 0,3
CO-Thin	248 ± 8	178 ± 6	78 ± 3	20,9 ± 0,6	13,8 ± 0,4	14,7 ± 0,4	4,9 ± 0,1
Fe-Thin	107 ± 3	74 ± 2	27,7 ± 0,8	9,0 ± 0,3	4,3 ± 0,1	6,0 ± 0,2	2,2 ± 0,1
Ni-Long	118 ± 4	79 ± 3	35 ± 1	14,2 ± 0,4	6,7 ± 0,2	7,8 ± 0,2	2,7 ± 0,1
Ni-Short	112 ± 2	75 ± 2	32 ± 0,6	14,0 ± 0,2	6,4 ± 0,1	7,6 ± 0,1	2,7 ± 0,1
Ni-DC	558 ± 25	460 ± 28	204 ± 18	93 ± 8	34 ± 3	39 ± 3	8,6 ± 0,5
Ni-Free	sat.	sat.	510 ± 10	260 ± 10	95 ± 4	88 ± 5	12 ± 1

Table 3.4: X-ray flux vs absorbers of different thickness, for all targets. Errors are statistical only.

ToF data: as previously mentioned, LEMO connectors at negative potential have been used as ion collectors. Signal from LEMO was amplified outside the vacuum chamber and sent to a digital oscilloscope, which measured and saved the signal. Time to signal peak was immediately displayed and recorded for focusing purposes.

Since a different file, with tens of thousand of entries, was created for each oscilloscope channel and each laser shot, it was necessary to develop a software tool to analyze and display the ToF data. As part of this thesis's work, a dedicated program was written using python language. For a given event, it calculates and subtracts the baseline signal, finds the time and amplitude of the signal's maximum, calculates the integrated signal charge, and draws a plot if requested. Given a set of events, it also allows to calculate mean and variance of those quantities.

While time to peak has been found to be useful for focus control, the main interest for ToF data is shape analysis. Signal from ions rises very quickly, in tens of nanoseconds, and then falls much more slowly, in several hundreds of nanoseconds. However, this analysis will be done in future and is not included in this thesis.

Chapter 4

Discussion

This work's data have been very useful to compare different targets vs bulk aluminum and among each other. This provides useful information for target optimization, and the next generation of targets will be produced taking these data into account.

In this chapter, data from irradiation of different targets will be discussed, comparing nanostructured targets among each other and with bulk aluminum. Finally, current results will be compared with literature.

4.1 Targets comparison

4.1.1 Overview

This work is aimed at finding optimal target parameters for plasma formation. So, targets were prepared with parameters (described in detail in section 2.1.2) chosen to allow six important comparisons:

- **Nanostructured vs bulk aluminum:** all targets nanostructured targets are compared to bulk-aluminum data.
- **NWs metal:** several kind of metals can be used to form NWs. Three very similar targets, Ni-Thin, Co-Thin and Fe-Thin, had been prepared to study the different response to irradiation. In future, more metals could be tested in similar conditions.
- **NWs diameter:** as previously explained, geometry of NWs strongly affects plasmonic coupling of light and propagation length. While choice of NWs diameter is limited by constraints in anodization conditions, different electrolytes allow to choose very different values. For this comparison, oxalic acid (Ni-Long target, 50 nm diameter) and sulphuric acid (Ni-Thin target, 20 nm diameter) have been used.

- **NWs length:** length of nanowires, which can be controlled by deposition time, is a parameter of great interest, since it can be finely tuned for optimization and could provide crucial insight on the phenomena occurring during irradiation. To allow a comparison between targets as similar as possible, NWs of different length have been grown on the same physical target by rising it partly out of the solution during electrodeposition. This way, two regions with NWs 5 and 10 μm long have been obtained (labelled Ni-Short and Ni-Long), with every other parameter being equal.

- **Electrical contact:** targets produced via AC and DC deposition differ mainly due to the continuous oxide layer between the NWs' bottom and the aluminum substrate, which is absent in DC deposited targets. This is of great interest, since plasmonic excitations could behave very differently when the metal is coupled with another metal instead of a dielectric. To study this effect, a single target with contacted NWs (Ni-DC) has been produced, with very similar parameters to the Ni-Long target, which is AC produced.

- **NWs confinement:** for DC targets, the alumina layer can be partially dissolved by a chemical attack without destroying the NWs (this cannot be done in AC targets, since AC deposited NWs are not coupled directly to the aluminum substrate and would collapse without alumina). The role of alumina in the laser-target interaction is important, since it affects plasma both propagation length and the dynamic of plasma formation, and very little studied in literature. To study it, alumina has been dissolved leaving "freestanding" NWs in target Ni-Free, liberated from alumina, to be compared with the "confined" ones.

4.1.2 Comparison with bulk aluminum

The advantage of producing plasma by irradiation of nanostructured targets instead of bulk metal ones is the very basis of this work. If the contribution of plasmonic effect to laser energy transport is not negligible, nanostructured targets should have deeper craters and higher X-ray fluxes, thanks to longer hydrodynamic plasma lifetime and more absorbed energy, compared to bulk aluminum.

As expected, of all considered targets Al-Bulk has the lowest mean value for crater depth (see fig 4.1). It also has a lower crater volume compared to most targets, exceptions being the iron NWs target and the freestanding NWs target (see section 2.1.2 for detailed description of targets), due to lower crater radius in those targets, but this is not surprising since lateral development of craters is not enhanced by plasmonic effect,

which transports energy only along the NWs. Also, greater volume does not necessarily imply greater plasma production, since matter can be removed at liquid or gaseous state.

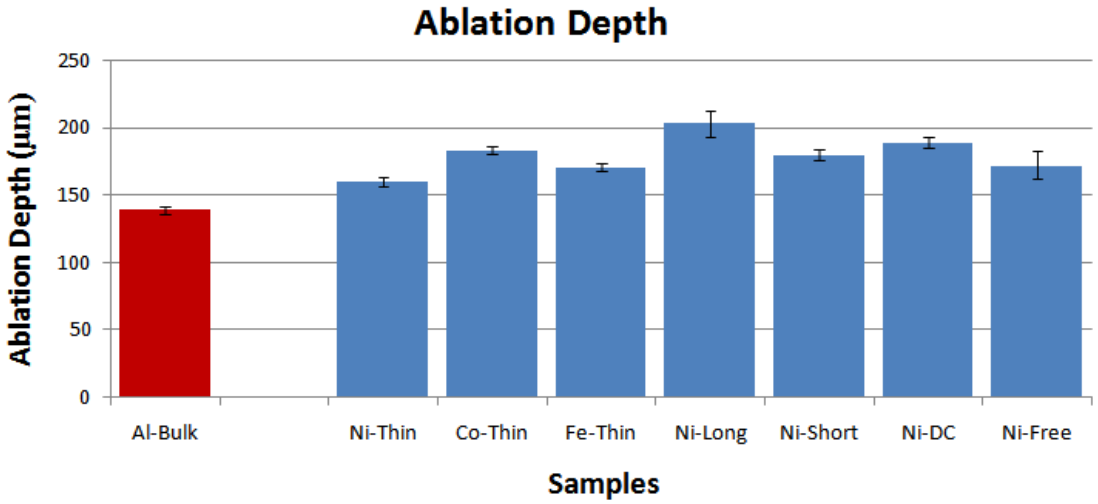

Figure 4.1: Ablation depth comparison between bulk aluminum (red) and nanostructured (blue) targets. Craters in aluminum were found to be considerably shallower than craters in nanostructured targets, with high significance. While the difference (15 to 45%) might seem comparatively small, it should be considered that ablation depth grows with square root of energy in ordinary targets

In figure 4.2, X-ray flux is compared among all targets. As can be seen, higher fluxes were measured for each nanostructured target than for the bulk aluminum target. The difference is largest for thin absorbers, but is still statistically significant for the thickest.

In figure 4.3, the X-ray flux for each nanostructured target is shown after normalisation to the bulk-aluminum flux.

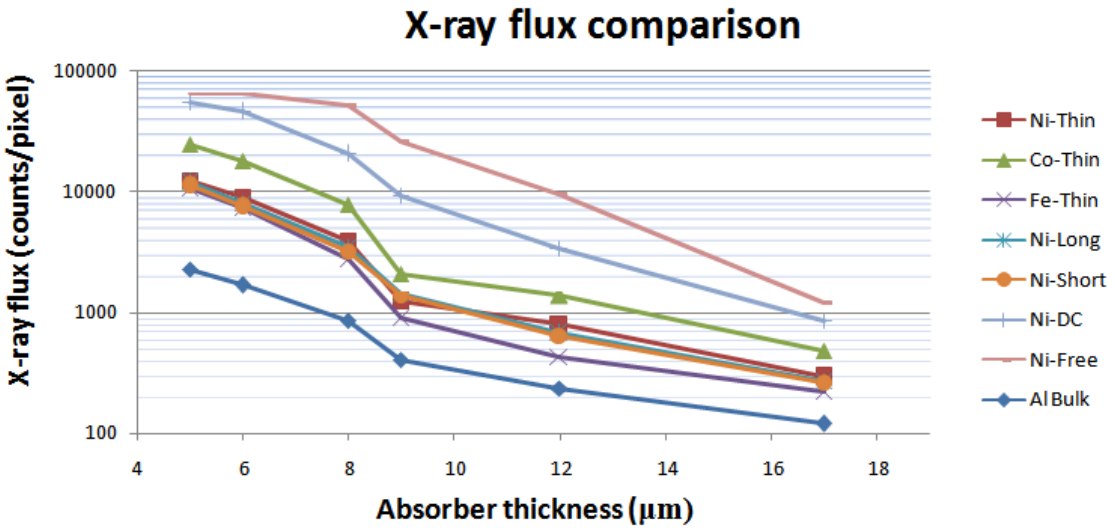

Figure 4.2: X-ray flux for each target. Note that for the first two points of Ni-Free target, CCD camera saturated, therefore the values in the graph should be considered lower limits. Note that all nanostructured targets have a flux greater than bulk aluminum. Log scale is used, since values range over two orders of magnitude. Error bars are not represented for clarity, but uncertainty is lower than 10% for all data points - see table 3.4

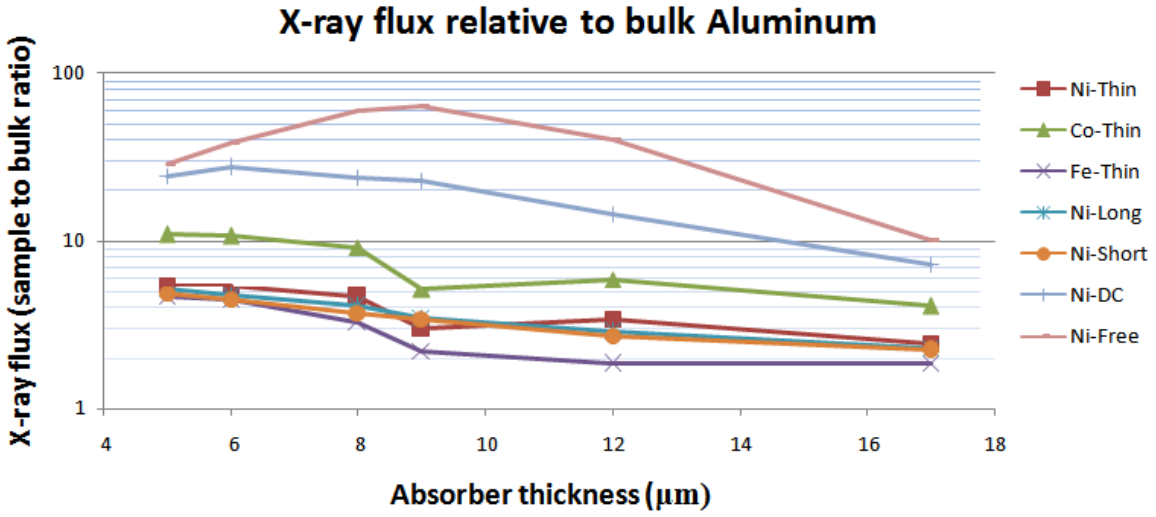

Figure 4.3: X-ray flux for each target, divided by bulk aluminum flux for each absorber. Note that most targets keep an almost constant ratio with bulk aluminum for most absorbers, then decrease for the thickest absorbers. Error bars are not represented for clarity.

The X-ray flux difference between bulk aluminum and nanostructured targets varies between a factor two and a factor sixty increase depending on target and absorber, with the highest gains for the two electrically contacted targets, Ni-DC and Ni-Free.

While data from the target with the highest X-ray flux, i.e. freestanding nanowires, should be considered with some caution (as will be discussed later), it can be concluded that laser irradiation of nanostructured targets yields a considerably greater X-rays flux

and leads to deeper ablation of matter.

While this analysis is aimed at comparison, and physical explanation of observed phenomena is left for future research, these data support the hypothesis of a deep energy transport into the matter due to plasmonic effect. Deeper penetration of energy could explain the increase in depth, while more energy absorption and longer hydrodynamic lifetime could explain the X-ray flux increase.

Interpretation of this result and its importance will be further discussed in the next section.

4.1.3 NWs metal

Three targets have been dedicated to the comparison of NWs metal.

As can be seen in table 4.1, craters in Co have been found with high significance to be both the deepest and greatest in volume. Both depth and volume are about 15% larger in the Co target than in Fe and Ni - indicating that most of the volume gain is due to deeper ablation, with little difference in crater radius.

Morphological data - NWs metal comparison				
	Co-Thin	Ni-Thin	Fe-Thin	Al-Bulk
Depth (μm)	184	160	171	139
σ depth (μm)	3	3	3	3
Δ depth (μm)	-	24	13	45
Significance ($\frac{D_x - D_{Co}}{\sigma_x}$)	-	5,1	2,8	9,6
Volume (μm^3)/10^6	4,52 $\cdot 10^6$	3,99 $\cdot 10^6$	3,39 $\cdot 10^6$	3,67 $\cdot 10^6$
σ volume (μm^3)/10^6	0,05	0,08	0,09	0,13
Δ volume (μm^3)/10^6	-	0,5	1,1	0,9 $\cdot 10^5$
Significance ($\frac{V_x - V_{Co}}{\sigma_x}$)	-	5,7	11	6,1

Table 4.1: Morphological comparison between targets with different NWs metals, plus Al-Bulk. Comparisons are relative to cobalt target values. Significance is calculated as parameter difference divided by squared sum of SDOM.

Considering X-ray fluxes, as shown in figure 4.4, Co is once again clearly superior to the other metals, with the highest flux of the three metal comparison targets for all absorbers, usually about twice the flux of the other two targets.

Considering the Ni vs Fe comparison, craters in Ni nanowires are shallower but greater in volume, since they have a considerably larger radius. This is partly because iron craters

have unusually small radius, and partly because craters in Ni NWs are subject to the previously mentioned "peeling off" of alumina, which contributes to volume but not to depth. On the other hand, targets with Ni NWs yield a greater X-rays flux, by 10 to 30% depending on absorbers. Although there is no conclusive indication of which is a more suitable NWs metal between Ni and Fe, Co is definitely preferable to both.

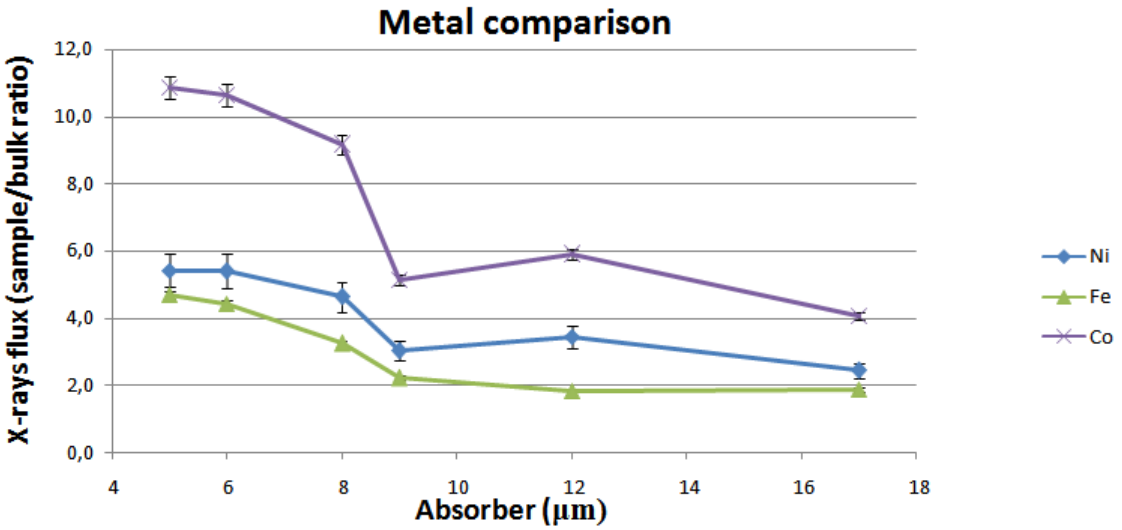

Figure 4.4: X-ray flux relative to Al-Bulk for targets with different NWs metal, vs absorber thickness. Note that flux for Co is greater than both other metals by a factor of 1.5 - 2 depending on absorber. The difference between Ni and Fe NWs is smaller, but flux from Ni NWs is consistently higher

These large differences in crater morphology and X-ray flux cannot be explained by the bulk propertiers of the metals, since they are quite close in terms of relevant physical properties like density, fusion and vaporization latent energies, and ionization energy. The difference could be due to better regularity and crystallinity of the Co NWs, or to an intrinsic advantage - for example greater propagation length - of Co NWs compared to Fe and Ni. It should be considered that Co has the highest electrical conductivity among the three metals, and that could mean less energy loss in plasmons propagation.

Unfortunately, most targets used in this work were filled with Ni. In future, cobalt will be the material of choice for nanostructured targets in this work, but more metals (Ag, Au, Cu) still need to be tested. Since more than one parameter could be material-dependent, like propagation length and photon-plasmon coupling efficiency, in future more tests will be performed to verify that Co NWs are preferable also for greater NWs length.

4.1.4 NWs diameter

The targets chosen for this comparison were Ni-Thin (sulphuric, $\approx$ 20 nm) and Ni-Long (oxalic, $\approx$ 50 nm). It should be noted that Ni-Long has a thicker alumina layer

compared to Ni-Thin, which could affect the reliability of the comparison.

As can be seen in 4.2, morphological data show a considerably superior depth for craters in Ni-Long.

Morphological data - NWs diameter comparison			
	Ni-Long (50 nm)	Ni-Thin (20 nm)	Al-Bulk
Depth (μm)	203	160	139
σ depth (%)	10	3	3
Δ depth (μm)		43	64
Significance ($\frac{D_x - D_{Long}}{\sigma_x}$)		4,1	6,1
Volume $(\mu m^3)/10^6$	5,3	3,99	3,7
σ volume $(\mu m^3)/10^6$	0,2	0,08	0,13
Δ volume $(\mu m^3)/10^6$	-	1,3	1,7
Significance ($\frac{V_x - V_{Long}}{\sigma_x}$)	-	5,2	6,0

Table 4.2: Morphological comparison between targets with different NWs diameter, plus Al-Bulk metal. Comparisons are relative to Ni-long values. Significance is calculated as parameter difference divided by squared sum of SDOM. Note that difference between targets are well beyond uncertainty for both diameter and depth

X-ray data (see figure 4.5) are less conclusive: for most data points, fluxes from the compared targets are equal within uncertainty. This is surprising, since the morphological difference is rather large. Is has been hypotized that in the deeper craters, plasma forms at greater depth, and is shielded by the surrounding material - it should be considered that the aluminum surrounding the craters is much thicker than the absorbers on the CCD camera, and absorbs almost completely X-rays in the few keV range, at least before plasma expands outside the crater..

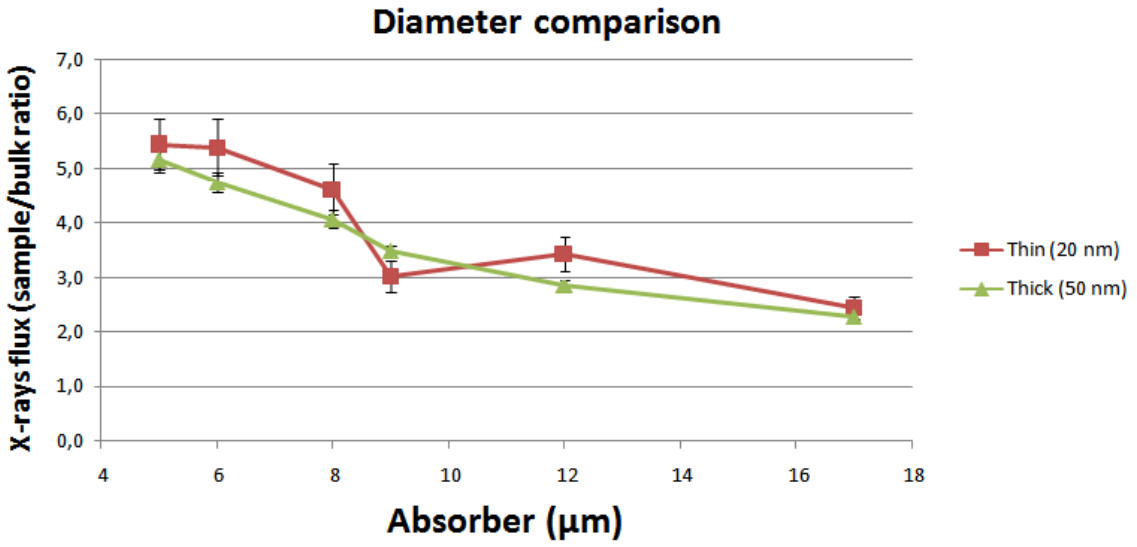

Figure 4.5: Integrated X-ray flux relative to Al-Bulk for targets with different NWs diameter, vs absorber thickness. While, in contrast with morphological data, X-ray flux is higher for most data points relative to Ni-Thin target, the differenc is quite small, and smaller than uncertainty for several data points.

The thicker alumina layer for Ni-Long target could have a role in shielding part of the X-rays from that target. If this was the case, though, some difference in X-ray flux would be expected at least for the thickest absorbers. The relationship between morphological and X-ray data will be discussed again further.

While this work main aim is to experimentally find the best target parameters, and physical interpretation of the results, is left to future research, some explanations have been proposed to account for the deeper ablation in large NWs diameter targets:

- Resonance effects: transmission of light through nanowires arrays has been demonstrated to have resonant peaks for wavelength multiple of the array period (interpore distance in our case, which is related to NWs diameter). Oxalic geometry might be closer to resonance conditions compared to sulphuric. This hypothesis could be tested in future changing the incident beam wavelength.

- Greater propagation length: as long as both are small compared to wavelength, NWs with larger radius are expected to have greater propagation length. Deeper energy transport could explain part of the difference in depth.

4.1.5 NWs length

For NWs height comparison targets Ni-Short and Ni-Long are used. It should be noted that the Ni-Long target has a low number of valid craters, due to a setup malfunction during its irradiation.

As can be seen in table 4.3 morphological data show a significant increase in depth and volume. Considering that the two targets differ only in NWs length, these data are a strong indication of deeper ablation for longer nanowires. This could be explained as a deeper transport of energy due to plasmonic effect.

Morphological data - NWs length comparison			
	Ni-Long (10 μm)	Ni-Short (5 μm)	Al-Bulk
Depth (μm)	203	180	139
σ depth (μm)	10	4	3
Δ depth (μm)	-	23	64
Significance ($\frac{D_x - D_{Long}}{\sigma_x}$)	-	4,3	6,1
Volume $(\mu m^3)/10^6$	5,3	4,67	3,67
σ volume $(\mu m^3)/10^6$	0,2	0,05	0,13
Δ volume $(\mu m^3)/10^6$	-	0,7	1,7
Significance ($\frac{V_x - V_{Long}}{\sigma_x}$)	-	2,6	6,0

Table 4.3: Morphological comparison between targets with different NWs length, plus Al-Bulk. Comparisons are relative to Ni-Long values. Significance is calculated as parameter difference divided by squared sum of standard deviations. Note that difference between targets is well beyond uncertainty for both diameter and depth

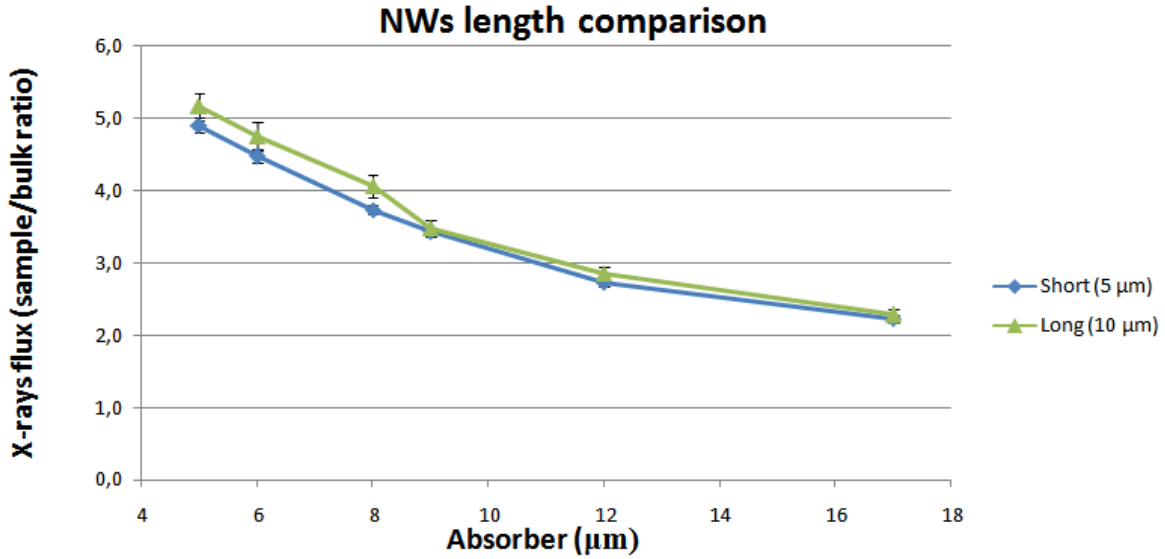

Figure 4.6: Integrated X-ray flux relative to Al-Bulk for targets with different NWs diameter, vs absorber thickness. In contrast with the strong morphological result, difference between data points is smaller than uncertainty for most absorbers.

X-ray data (see figure 4.6) are much less conclusive - while Ni-Long has a higher average flux for each absorber, the difference is not statistically significant for most data points.

Therefore, fabricating longer NWs seems important for future data takings.

4.1.6 AC vs DC deposition

Target Ni-DC has been fabricated via direct current electrodeposition, instead of alternate current like all the other targets. Therefore, for DC targets, there is no continuous oxide layer between the base of NWs and the aluminum substrate, and NWs are in electrical continuity with the metal substrate.

AC/DC comparison is based on targets Ni-DC and Ni-Long. As can be seen in table 2.1, except for deposition mode, they have identical nominal parameters ($\approx$ 50 nm diameter, 10 μm long NWs).

Morphological data (table 4.4) show peculiar results: difference in depth is below statistical significance, while crater volume is considerably larger for the DC target.

Morphological data - deposition mode comparison			
	Ni-DC	Ni-Long (AC)	Al-Bulk
Depth (μm)	189	203	139
σ depth (μm)	4	10	3
Δ depth (μm)		-14	50
Significance ($\frac{D_x - D_{DC}}{\sigma_x}$)		1,3	9,9
Volume (μm^3)/10^6	4,20	5,3	3,67
σ volume (μm^3)/10^6	0,07	0,05	0,13
Δ volume (μm^3)/10^6	-	-1,1	0,52
Significance ($\frac{V_x - V_{DC}}{\sigma_x}$)	-	4,5	3,6

Table 4.4: Morphological comparison between targets with different deposition modes, plus Al-Bulk. Comparisons are relative to Ni-DC values. Significance is calculated as parameter difference divided by squared sum of SDOM. While depth difference is below uncertainty, there is a large difference in volume.

X-ray data (figure 4.7) show an exceptional flux for the DC target, five times higher than the AC target. Therefore DC deposition seems a promising approach for future targets.

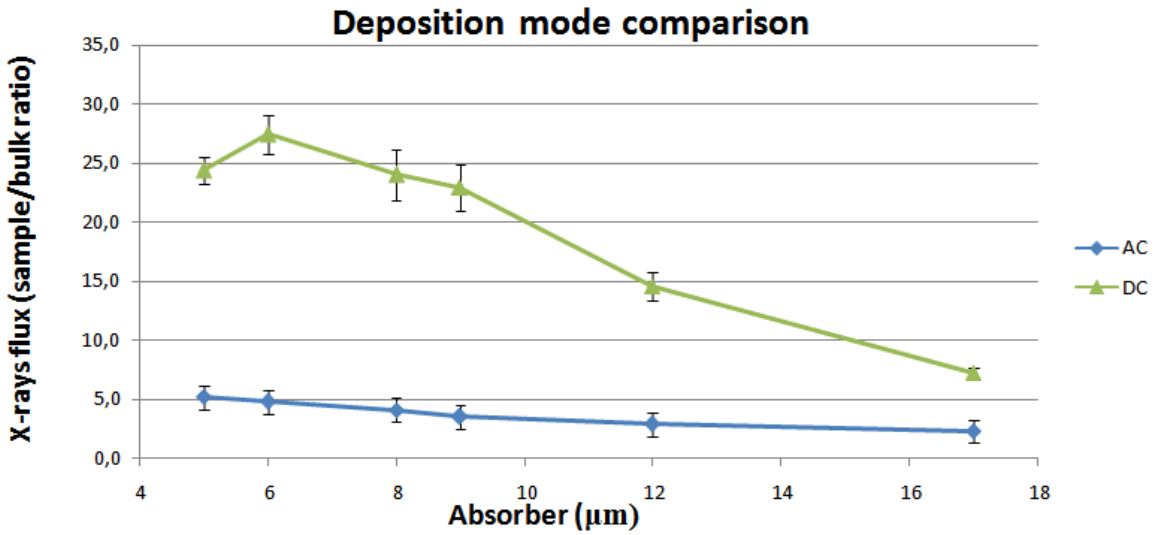

Figure 4.7: Integrated X-ray flux relative to Al-Bulk for targets with different deposition mode, vs absorber thickness. In contrast with the inconclusive morphological data, an exceptional X-ray flux (30 times greater than Al-Bulk values) is found for the DC deposited NWs. The difference between targets is many times larger than uncertainty.

4.1.7 Confined vs freestanding NWs

Ni-DC and Ni-Free are compared to study the effect of the alumina layer on laser-target interaction. Since Ni-Free target has been obtained by chemically removing alumina on the same physical sample of Ni-DC, except for confinement the two targets are identical.

Morphological data - NWs confinement comparison			
	Ni-Free	Ni-DC (Confined)	Al-Bulk
Depth (μm)	172	189	139
σ depth (μm)	10	4	3
Δ depth (μm)		-17	33
Significance ($\frac{D_x - D_{Conf}}{\sigma_x}$) ($\mu$m)		1,5	6,6
Volume (μm^3)/10^6	3,7	4,20	3,67
σ volume (μm^3)/10^6	0,2	0,07	0,13
Δ volume (μm^3)/10^6	-	-2,1	0,1
Significance ($\frac{V_x - V_{Conf}}{\sigma_x}$)	-	4,5	3,6

Table 4.5: Morphological comparison between confined and freestanding NWs, plus Al-Bulk. Comparisons are relative to Ni-DC values. Significance is calculated as parameter difference divided by squared sum of standard deviations. While depth difference is below uncertainty, there is a large difference in volume.

As can be seen in table 4.5, confined craters show a slightly larger (not statistically significant) depth and much larger volume. Free NWs craters have smaller volume compared to any other sample. This is probably due to the reduced thermal conduction and shockwave propagation in absence of the alumina matrix.

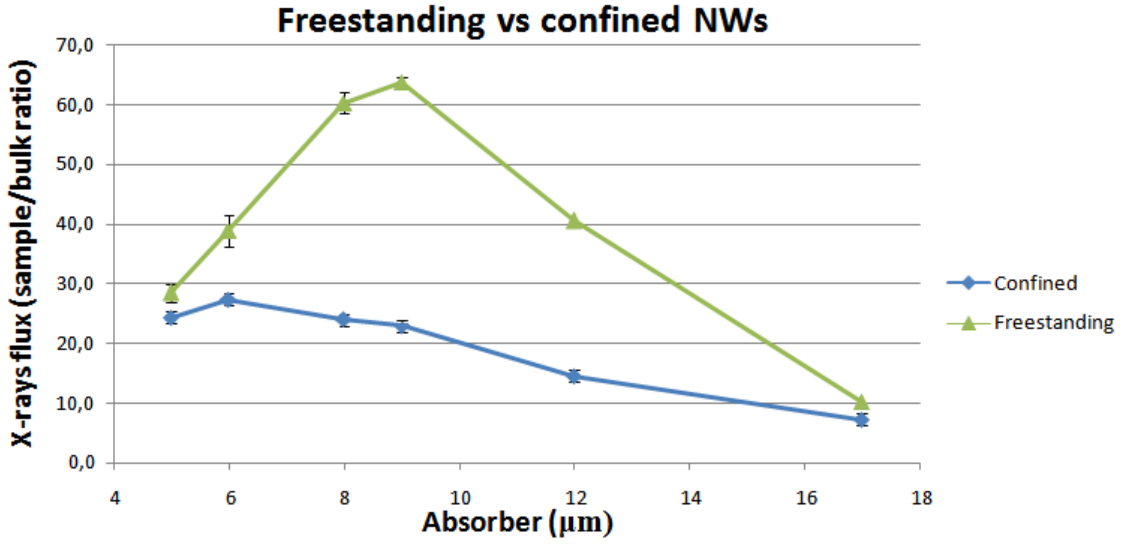

Figure 4.8: Integrated X-ray flux relative to Al-Bulk for freestanding and confined NWs, vs absorber thickness. For the two thinnest absorbers, Ni-Free data is affected by CCD pixel saturation, and should be considered a lower limit. The flux from the freestanding NWs target is larger than that from the confined NWs by a factor of two. Note that both fluxes are exceptional compared to Al-Bulk.

X-ray data (see fig 4.8) show a mean flux much higher (by more than a factor of 2) for the free NWs target, compared to the flux of the confined NWs region - making it by far the highest X-ray flux in any target tested during this phase.

While this is an interesting result, it should be considered that the almost complete lack of oxide layer in the free NWs region is very likely to lead to a higher measured flux due to a reduced self-shielding. On the other hand, some difference in fluxes ratio would be expected for different absorbers, since the total thickness of the oxide layer is comparable to the thickest absorber. While there is a small decrease in ratio for the two thickest absorbers, it is a feature common to several targets, and count rates for thickest fluxes are limited by comparatively low statistics.

From a target production point of view, it is not yet clear if freestanding NWs are a more attractive target for plasma production compared to confined ones, but the high X-ray flux is promising, and understanding the differences between freestanding and confined nanowires could lead crucial insight on the role of the oxide layer in plasma formation. Therefore, since DC targets have proved to be highly promising, part of their surface will likely be dedicated to free NWs production.

4.2 Comparison summary

In table 4.6, a summary of the performed comparisons is presented. For each compared parameter, the target type with greatest measured X-ray flux and ablation depth are shown. Since volume seems to be a less useful parameter compared to depth, it is not considered in this table.

Samples comparison overview			
Parameter	Compared NWs types	Max depth	Max X-ray
Metal type	Co, Ni, Fe	Co	Co
NWs diameter	20 vs 50 nm	50 nm	Inconclusive
NWs height	5 vs 10 μm	10 μm	Inconclusive
NWs deposition mode	AC vs DC	Inconclusive	DC
NWs confinement	confined vs freestanding	Inconclusive	Freestanding

Table 4.6: Overview of comparisons between nanostructured targets. For each comparison, the target type which yielded the maximum depth and that which yielded the largest X-ray flux is listed. Since the control over targets parameters and systematics error was not perfect, X-ray flux differences lower than a factor of two and depth difference smaller than three times the total uncertainty are considered inconclusive.

Note that only significant results are reported - that is, X-ray flux difference by at least a factor of two for the majority of absorbers and mean depth difference significant at three sigma or higher.

It is evident that X-ray and depth results seem to be complementary. Except for metal comparison, on which both show the same result, they seem to react to different variables. This is in itself a result of great interest, and a target for future research.

As for construction of future targets, oxalic acid anodization followed by cobalt deposition seems to be the best choice for future targets. Targets with longer NWs, searching for an optimal length, will very likely be included in future data takings.

Production of NWs contacted to metal, via DC deposition, seems also very promising, especially considering it allows to obtain freestanding NWs by chemical removal of alumina.

4.3 Interpretation of results

While this work is aimed at comparative observation of targets, and detailed explanation of the physics behind the observed differences is left for future research, one very important question must be addressed: is there supporting evidence for a role of nanostructures in the plasma formation process?

As demonstrated in detail in section 4.1.2, both morphological and X-ray data show considerable improvement for all nanostructured targets compared to Al-Bulk. This, however, does not necessarily imply a role for the nanostructures: the presence of metal and oxide in the target surface could change the laser-target interaction, independently of their structures.

While a reference target with anodized aluminum but no deposited metal was irradiated during a preliminary data taking, and performed considerably worse than nanostructured targets, no control sample with the exact chemical composition of the nanostructured targets has been realized.

While the fraction of metal in the target surface is quite low (only 10 to 15% of the oxide layer is filled with metal, and the oxide layer is less than 10% of typical craters' depth), metals such as Ni and Co have an X-ray conversion efficiency almost ten times higher than aluminum (see figure 4.9), so even in small quantities they could increase X-ray emission.

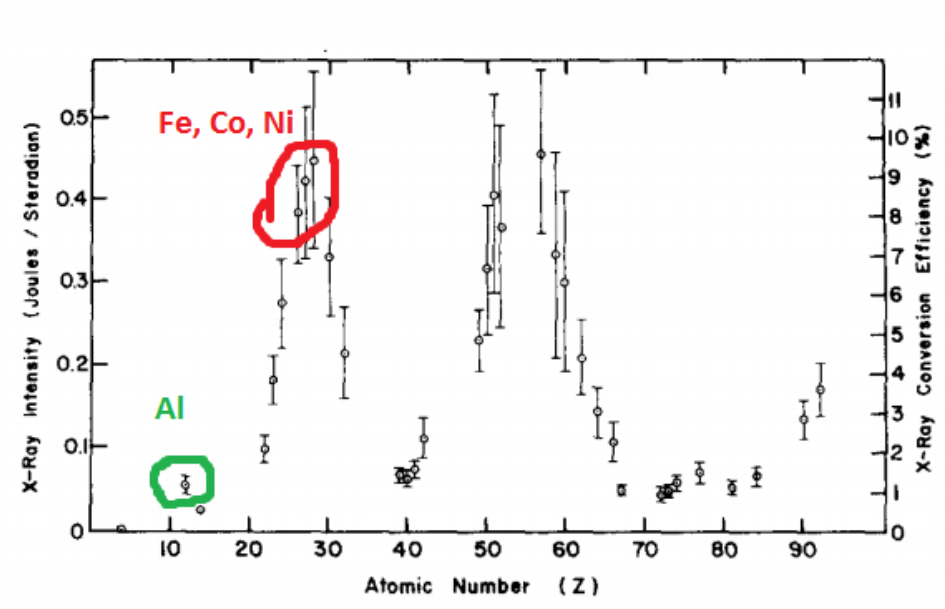

Figure 4.9: X ray conversion efficiency of laser light, experimentally measured [37] using an 8 ns laser focused to $4 \cdot 10^{13} W/cm^2$. As can be seen, aluminum (highlighted in green) has a lower conversion efficiency by almost a factor of ten compared to the metal used for NWs (highlighted in red). Despite the low concentration of NWs metal in the ablated volume, this could explain part of the observed X-ray flux increase. However, Ni, Co and Fe have very similar conversion efficiency (Ni having the highest of the three), while a much greater X-ray production was observed for the target with CO NWs .

Also, it must be considered the targets are much less reflective than bulk aluminum, and while this is a consequence of their nanostructures, if the advantages of nanostructured targets depended only on their colour, a thin dark coating on bulk metal would be much more simple and economical to realize.

However, while targets' comparison with bulk aluminum could be explained to some

extent by different chemical composition and lower reflectivity, this argument does not hold for the comparison between nanostructured targets themselves.

For example, the difference in relevant physical properties for Ni, Co and Fe is very small - they have very similar X-ray yield when irradiated in their pure forms (see figure 4.9), they have very close vaporization and ionization energy, and being consecutive in the periodic table they have very little difference in density and atomic number. Yet, Fe and Co NWs show a 15% difference in depth and a factor two difference in X-ray flux.

Moreover, the comparison between contacted and non contacted NWs should be considered. Targets with contacted (DC deposited) and non contacted (AC deposited) NWs are very different when their nanostructures are taken into account: contacted NWs are continuous with the aluminum substrate, while non contacted NWs are insulated. Also, since different deposition solutions and electrical parameters are used, they could have different crystallinity and purity.

But without accounting for this nanoscale differences, the compared DC and AC targets are almost identical: they have the same amount of deposited metal (except for fluctuations in the fabrication process) at the same depth, and they have nearly identical thickness of oxide layer. When irradiated, DC targets yield a greater X-ray flux by a factor of five. While the exact physics beyond this difference is still to be understood, it cannot be explained by the bulk properties of aluminum, nickel and oxygen, without considering the nanostructures involved.

While not conclusive, the large X-ray flux difference between AC and DC targets is also supporting evidence for energy transport along the NWs. If energy from the laser was deposited only in the first nm of the target surface, as would be with a bulk target, the resulting X-ray flux should not be affected by the presence of an oxide layer several μm beneath. Still, it is not yet possible to exclude different contributions, for example better regularity and fewer impurities in DC produced targets.

In conclusion, while the exact physical processes involved in laser ablation of nanostructures are beyond the scope of this work, the observed data cannot be explained considering only the bulk behavior of the elements in the targets, and the transport of energy along nanowires is likely to play a role in it.

4.4 Literature comparison

Very little data can be found in literature regarding laser ablation of metallic nanowires in allumina. Only one dedicated study was found, by Purvis *et al* (see reference [23]), published in 2013.

The comparison is very interesting, both for the similarities and differences in results.

The target described by Purvis *et al* is remarkably similar to this work's in several aspects: nanowires of comparable geometrical parameters (Ni and Au in their case) were produced by electrodeposition in nanoporous alumina templates, freed for alumina, and irradiated with a joule laser. The most important difference is the laser pulse length: while a 6 ns laser was employed in this work, Purvis *et al* used a 60 fs laser, five orders of magnitudes shorter, with intensity $5 \cdot 10^{18} W/cm^2$.

While Purvis *et al* did not include any morphological analysis and focus on absolute plasma parameters, they report a 50-fold increase in total X-ray flux, which is comparable to the most promising result presented in this thesis, that from freestanding nickel NWs..

However, from the simulations they performed, they predict that this flux increase should be critically dependent on laser pulse duration. According to their analysis, after just 300 fs the nanowires should be destroyed, and energy would no longer be transported inside the material. According to this prediction, a longer laser pulse would couple only with disordered plasma, and therefore nanostructured targets should not perform significantly better than non-nanostructured targets of similar elemental composition.

Since only a negligible percentage of the 6 ns energy pulse could reach the target in 300 fs, this is obviously in contrast with our observations.

As explained in the last section, the difference in observed parameters for our targets cannot be explained as arising from bulk properties of the elements involved - especially considering metal comparison and contacted vs non contacted nanowires comparison. Therefore, it seems very unlikely that nanostructures are destroyed before a significant fraction of the laser energy is delivered.

While papers describing laser ablation of bulk targets [30] report comparable ablation efficiency for fs and ns laser in the IR wavelength range, that result is explained as laser coupling to low density plasma, which should not be sensitive to the presence of nanostructures.

However, the prediction of nanostructured losing any advantage for longer pulses is based on simulations and not experimental data. Since our experiment provides strong support for the hypothesys of plasma parameters being sensitive to nanostructures, it appears the current understanding of plasma formation on nanostructured targets (a very new field, with very little experimental data) is limited.

The role of the alumina layer - which has a much greater latent fusion heat compared to NWs metal, and a much longer thermalization time - might be important, and from this reseach no theoretical or experimental study has been dedicated to the interaction of energetic laser pulses and a metal-oxide composite nanomaterial such as the one employed in this work.

Since nanomaterials often exhibit very different properties compared to their con-

stituent materials, it is possible that accounting for both alumina and NWs is necessary to correctly understand the process. However, it should be considered that a very strong flux was obtained for the target with freestanding NWs, therefore the alumina confinement cannot be the only factor involved in NWs survival for longer times than expected.

This thesis work was comparative in nature, and while its results support the energy transport by NWs, not enough data are available to reconstruct the dynamics of plasma development. Since this is a very promising avenue of research for laser plasma production, in future both experimental and theoretical work will be required to refine the current understanding of laser plasma production on nanostructured targets.

4.5 Future developments

This thesis was part of a preliminary study for a new experiment, specifically aimed at optimization of nanostructured targets, and demonstration of technological applications for astrophysics and nuclear research.

Nanostructured targets could be interesting for this kind of research thanks to the more energetic plasma they can produce compared to bulk targets, and to the evidence of longer lived plasma reported by preliminary study of ToF data (see [24]).

In any case, further research is needed to continue the target optimization study started with this thesis and to understand the underlying physical processes. Some of the most important questions left open by this work, which future experiments should be able to answer, are:

- Whether other metals perform better than those already tested.
- If, and to what extent, ablation parameters can be improved further by longer nanowires.
- What is the dynamic of plasma formation - where does it begin, how long nanostructures survive, how does the laser pulse couple with the resulting plasma.
- Why X-ray flux and depth are sensitive to different target parameters.
- What plasma parameters (temperature, density, degree of ionization) can be reached by laser irradiation of nanostructures, and how they compare to bulk targets in absolute terms.

To answer this important questions, several proposal have been made for future experimental phases:

- Detailed information about X-ray spectra would greatly improve understanding of the produced plasma, since it would allow direct measurement of degree of ionization. From degree of ionization, plasma temperature can be calculated by the ratio of different ionization level of the same element (since it is dependent on temperature only). Single photon counting in the CCD camera is expected to allow spectral analysis of X-ray fluxes in future.

- Time resolved data from ICCD camera, ion collectors and scintillator must be analyzed and compared to understand as well as possible the dynamics of plasma formation, especially in the first nanoseconds after the beginning of the laser pulse.

Chapter 5

Conclusions

This thesis studied the effects of pulsed laser irradiation on nanostructured targets, with a pulse duration of 6 ns and a power density of about $4 \cdot 10^{12}$ W/cm^2, with the goal to produce a dense, hot plasma, of great interest for astrophysics and nuclear physics studies. Results for different targets are compared in terms of ablation depth and X-ray emission of the produced plasma.

The nanostructured targets used in this study are metamaterials consisting in aligned metal nanowires grown by electrodeposition into a porous alumina matrix, obtained on a thick aluminum substrate. These materials were developed with specific geometrical parameters in order to maximize absorption in the visible and IR wavelengths.

In particular, to study which parameters lead to highest X-ray flux and ablation efficiency, nanowires were produced with different length, diameter, metal and deposition technique.

Large differences have been found both in X-ray fluxes and ablation efficiency among the studied targets. All nanostructured targets have shown a large increase in both X-ray fluxes and ablation efficiency compared to bulk aluminum. Also among nanostructured targets, large differences have been found. In particular, cobalt nanowires have been found to give a two-fold increase in X-ray flux compared to nickel and iron nanowires.

An even larger difference, a factor of five, has been obtained when two different nanowires deposition techniques, alternate current vs direct current, are applied. For DC deposition, each nanowire is electrically connected to the aluminum substrate, while for AC deposition nanowires are isolated from the substrate by a non-conductive alumina layer.

These differences in X-ray flux and ablation efficiency cannot be easily explained considering only the bulk properties of the elements present in the targets, like different atomic number and thermal conductivity of the nanowires. Nor can they be explained considering only the different reflectivity of targets, since all nanostructured targets had

an absorbance greater than 95% in the visible range and about 80% at the laser wavelength (1064 nm).

A possible explanation for the observed differences is that the so-called plasmonic effect plays an important role in electromagnetic energy absorption. Due to this effect, the light pulse is converted into an electrical pulse (at the top of the nanowire) and propagated along the nanowire. The adopted nanowires are tens of μm long, therefore the electromagnetic energy can be transported deeply into the material. Such a deep penetration is not possible in bulk materials, where energy is absorbed within the first 100 nm.

If this is the case, differences among targets could be explained in terms of different plasmonic propagation lengths, which is dependent on geometrical parameters of the nanowires - with large differences due to resonant absorption - and electrical conductivity.

Results presented in this thesis are consistent with those for laser ablation of Ag nanowires, published by Lanzalone *et al* in reference [35], which is based on preliminary tests with the same setup described in this work. That work also reports evidence of plasma stagnation for nanostructured targets.

Research published by Purvis *et al* [23] using similar targets, but a much shorter laser pulse ($\approx$ 30 fs), reports a factor 50 increase in X-ray flux from Au NWs. Results of this thesis seem to be in contrast with the hypothesis by Purvis *et al* that sub-picosecond laser pulse duration is an essential requirement for laser interaction with nanostructures.

This work is part of a preliminary study for a laser-plasma experiment, which will further improve target optimization, and study the processes involved in laser plasma production on nanostructured targets. Improved setup and detectors will allow to measure absolute plasma parameters such as density and temperature, and to study the time evolution of plasma, and the underlying physics.

In future, it is hoped this preliminary study will lead to progress for any application which requires a dense, hot and confined plasma, such as X-ray imaging and nuclear physics research.

Bibliography

[1] C. T. Sousa, D. C. Leitao et al.: "Nanoporous alumina as templates for multifunctional applications" - *Applied Physics Review 1 (2014): 031102*

[2] Mariana P. Proencaa, Célia T. Sousaa, João Venturaa, Manuel Vazquez, João P. Araujoa: "Ni growth inside ordered arrays of alumina nanopores: Enhancing the deposition rate" - *Electrochimica Acta 72 (2012): 215*

[3] L.Malferrari, A. Jagminien, G. P. Veronese, F. Odorici, M. Cuffiani, and A. Jagminas: "Alumina Template-Dependant Growth of Cobalt Nanowire Arrays" - *Journal of Nanotechnology (2009): 149691*

[4] Feiyue Li, Lan Zhang, and Robert M. Metzger: "On the Growth of Highly Ordered Pores in Anodized Aluminum Oxide" - *Chem. Mater. 10 (1998): 2470*

[5] "Anodic oxidation of Aluminum and its alloys" In Information Bulletin, vol. 14. London: The Aluminum development association, 1948.

[6] J. Choi, "Functional nanostructures by ordered porous templates" Ph.D. thesis, Martin-Luther University, 2004.

[7] Masuda H, Fukuda K, "Ordered metal nanohole arrays made by a two-step replication of honeycomb structures of anodic alumina." - *Science 268, (1995)*

[8] K. Nielsch, J. Choi, K. Schwirn, R. B. Wehrspohn, and U. Gosele, "Self-ordering Regimes of Porous Alumina: The 10% Porosity Rule" - *Nano Lett. 2, 677 (2002)*

[9] G. D. Sulka and K. G. Parkola, "Structural features of self-organized nanopore arrays formed by anodization of Aluminum in oxalic acid at relatively high temperatures"- *Electrochimica Acta 52, 1880 (2007)*

[10] Z. X. Su, G. Hahner, and W. Z. Zhou, "Electrochemical Anodizing, Structural and Mechanical Characterization of Nanoporous Alumina Templates"- *J. Mater. Chem. 18, 5787 (2008).*

[11] Tajima, "Luminescence, breakdown and colouring of anodic oxide films on Aluminum" - *Electrochim. Acta 22, 995 (1977).*

[12] S. Lal, S. Link, and N. J. Halas, "Nano-optics from sensing to waveguiding" - *Nature photonics 1, (2007): 641*

[13] A. W. Sanders, D. A. Routenberg, B. J. Wiley *et al*, "Observation of Plasmon Propagation, Redirection, and Fan-Out in Silver Nanowires" - *Nano Letters vol.6, n.8 (2006)*

[14] Logeeswaran VJ, J. Oh, A. P. Nayak, *et al*, "A Perspective on Nanowire Photodetectors: Current Status, Future Challenges, and Opportunities" - *IEEE Journal of selected topics in quantum electronics 17.4 (2011)*

[15] Atwater, Harry A., and Albert Polman. "Plasmonics for improved photovoltaic devices." - *Nature materials 9.3 (2010): 205-213.*

[16] Wang, Wenhui, et al. "Light propagation in curved silver nanowire plasmonic waveguides." - *Nano letters 11.4 (2011): 1603-1608.*

[17] Lima, Joaquim, et al. "Optical properties of nanowire metamaterials with gain." - *Optics Communications 379 (2016): 25-31.*

[18] Malferrari, L., et al. "Alumina Template-Dependant Growth of Cobalt Nanowire Arrays." - *Journal of Nanotechnology 2009 (2009)*

[19] Yan, Ruoxue, et al. "Direct photonic–plasmonic coupling and routing in single nanowires." - *Proceedings of the National Academy of Sciences 106.50 (2009): 21045-21050.*

[20] Ditlbacher, Harald, et al. "Silver nanowires as surface plasmon resonators." - *Physical review letters 95.25 (2005): 257403.*

[21] Michael Antony Purvis PhD Dissertation, "relativistic plasma nano-photonics for ultra-high ehergy density physics" - *Colorado State University): 2014*

[22] Brown, Matthew S., and Craig B. Arnold. "Fundamentals of laser-material interaction and application to multiscale surface modification." chapter 4. Springer Berlin Heidelberg, 2010: 91-120.

[23] Purvis, Michael A., et al. "Relativistic plasma nanophotonics for ultrahigh energy density physics." - *Nature Photonics 7.10 (2013): 796-800.*

[24] Lanzalone, G., et al. "Effect of advanced nanowire-based targets in nanosecond laser-matter interaction." - *Review of Scientific Instruments 87.2 (2016): 02B324.*

[25] Jafarabadi, Marzieh Akbari, and Mohammad Hossein Mahdieh. "Investigation of phase explosion in Aluminum induced by nanosecond double pulse technique." - *Applied Surface Science 346 (2015): 263-269.*

[26] Torrisi, L., A. Borrielli, and D. Margarone. "Study on the ablation threshold induced by pulsed lasers at different wavelengths." - *Nuclear Instruments and Methods in Physics Research Section B: Beam Interactions with Materials and Atoms 255.2 (2007): 373-379.*

[27] Luca U. Labate PhD dissertation, "Progress in laser-plasma X-ray sources: time-resolved spectroscopic studies and applications to µ-imaging" - *Università degli studi di Bologna, 2004*

[28] Margarone, D., et al. "Studies of craters' dimension for long-pulse laser ablation of metal targets at various experimental conditions." - *Applied Surface Science 254.9 (2008): 2797-2803.*

[29] Salle, B., et al. "Laser ablation efficiency of metal samples with UV laser nanosecond pulses." - *Applied surface science 138 (1999): 302-305.*

[30] Semerok, Alexandre F., et al. "Microablation of pure metals: laser plasma and crater investigations." Nonresonant Laser-Matter Interaction (NLMI-10). - *International Society for Optics and Photonics, 2001.*

[31] Price, D. F., et al. "Absorption of ultrashort laser pulses by solid targets heated rapidly to temperatures 1–1000 eV." - *Physical review letters 75.2 (1995): 252.*

[32] Mahdieh, M. H., et al. "Crater geometry characterization of Al targets irradiated by single pulse and pulse trains of Nd: YAG laser in ambient air and water." - *Applied Surface Science 256.6 (2010): 1778-1783.*

[33] Ruoxue Yan, Peter Pausauskie, Jiaxing Huang, and Peidong Yang: "Direct photonic–plasmonic coupling and routing in single nanowires" - *PNAS vol. 106 no. 50 (2009): 21045*

[34] Michael A. Purvis, Vyacheslav N. Shlyaptsev *et al*: "Relativistic plasma nanophotonics for ultrahigh energy density physics" - *Nature - photonics, vol 7 (2013): 796*

[35] G. Lanzalone, C. Altana *et al*: "Effect of advanced nanowire-based targets in nanosecond laser—Matter interaction" - *Review of Scientific Instruments 87 (2016)*

[36] H.J. Assenbaum and K. Langanke: "Effects of Electron Screening on Low-Energy Fusion Cross Sections " - *Z. Phys. A 327 (1987): 461*

[37] Glibert, K. M., *et al.* "X-ray yields of plasmas heated by 8-nsec neodymium laser pulses." - *Journal of Applied Physics 51.3 (1980): 1449.*